Precise predictions and new insights for atomic ionization from the Migdal effect

Peter Cox,[1,*] Matthew J. Dolan,[1,†] Christopher McCabe,[2,‡] and Harry M. Quiney[3,§]

[1]*ARC Centre of Excellence for Dark Matter Particle Physics, School of Physics, The University of Melbourne, Parkville, Victoria 3010, Australia*

[2]*Theoretical Particle Physics and Cosmology Group, Department of Physics, King's College London, London WC2R 2LS, United Kingdom*

[3]*School of Physics, The University of Melbourne, Parkville, Victoria 3010, Australia*

(Received 18 September 2022; accepted 12 January 2023; published 27 February 2023)

The scattering of neutral particles by an atomic nucleus can lead to electronic ionization and excitation through a process known as the Migdal effect. We revisit and improve upon previous calculations of the Migdal effect, using the Dirac-Hartree-Fock method to calculate the atomic wave functions. Our methods do not rely on the use of the dipole approximation, allowing us to present robust results for higher nuclear recoil velocities than was previously possible. Our calculations provide the theoretical foundations for future measurements of the Migdal effect using neutron sources, and searches for dark matter in direct detection experiments. We show that multiple ionization must be taken into account in experiments with fast neutrons, and derive the semi-inclusive probability for processes that yield a hard electron above a defined energy threshold. We present results for the noble elements up to and including xenon, as well as carbon, fluorine, silicon and germanium. The transition probabilities from our calculations are publicly available.

DOI: 10.1103/PhysRevD.107.035032

I. INTRODUCTION

Despite decades of searching, the precise nature of particle dark matter (DM) remains an enduring mystery. There is a wide-ranging program of direct detection experiments dedicated to measuring the properties of astrophysical DM in terrestrial laboratories [1]. These are based primarily on the possibility that DM scatters and imparts an $\mathcal{O}(\mathrm{keV})$ kinetic energy to an atomic nucleus. However, for DM masses less than a few GeV this method loses sensitivity, since the nuclear recoil energy becomes smaller than the experimental energy threshold.

An alternative approach for DM direct detection is to search for electromagnetic signals that may be produced when the DM interacts with the atomic nucleus [2–5]. The possibility that an electron may be emitted from an atom after the sudden perturbation of the nucleus has been known since the early 1940s [6–9] and has become known as the 'Migdal effect' within the DM community [5]. The broader importance of the Migdal effect for direct detection searches has only recently been established in [10,11], and further studied in [12–23]. Although the production of electromagnetic signals is suppressed relative to the rate of conventional elastic nuclear scattering, there is a window for sub-GeV DM where the nuclear recoil energy falls below threshold while the electromagnetic signal remains observable.[1] Several experiments have now exploited this to constrain the sub-GeV DM parameter space [29–36].

Despite the importance of the Migdal effect for DM searches, the emission of an electron after a sudden jolt to the nucleus by an electrically-neutral projectile has not been measured experimentally.[2] This has motivated several experimental proposals that aim to systematically study the Migdal effect over a wide range of energies and with different atomic species [46–48]. The proposals follow the standard practice within the DM community of using neutrons as the electrically-neutral proxy for DM and cover a range of neutron energies from 17 keV in Ref. [47],

*peter.cox@unimelb.edu.au
†dolan@unimelb.edu.au
‡christopher.mccabe@kcl.ac.uk
§quiney@unimelb.edu.au

[1]Polarization (or atomic) bremsstrahlung produces a similar effect [24–28], but its rate is suppressed relative to the Migdal effect [14].

[2]The Migdal effect has been measured experimentally in related scenarios where the recoil is due to α-decay [37–40] or β-decay [41–45].

565 keV in Ref. [46], to 2.5 MeV and 14.7 MeV in the MIGDAL experiment [48].

The characteristic signal of the Migdal effect is a recoiling ion and an ionization electron emerging from a common vertex. While the use of lower-energy neutrons allows the Migdal effect to be studied in the kinematic regime relevant for DM experiments, it has the disadvantage that the nuclear recoil and ionization electron cannot be separately resolved, either spatially or energetically; precise modeling of nuclear recoil quenching and the detector response is then required to test the Migdal effect (see e.g., [49,50]). In contrast, higher-energy neutrons probe a different energy regime from DM experiments, yet offer the possibility of indirectly or directly imaging the Migdal effect; indirectly in high-pressure gas, where the Migdal effect followed by de-excitation of the atom induces a 'two-cluster' topology [46]; and directly in low-pressure gas, where nuclear recoil and ionization electron tracks can be imaged emerging from a common vertex [48].

The qualitatively different scattering regimes for DM and neutron scattering are illustrated in Fig. 1. This figure also introduces the dimensionless ratio v/α, the magnitude of the nuclear recoil velocity relative to the fine-structure constant multiplied by the speed of light (we work in natural units with $\hbar = c = 1$), which will serve as a key parameter. While DM direct-detection experiments operate in the regime $v \ll \alpha$, neutron experiments can potentially test a much wider parameter space, up to $v \simeq \alpha$.

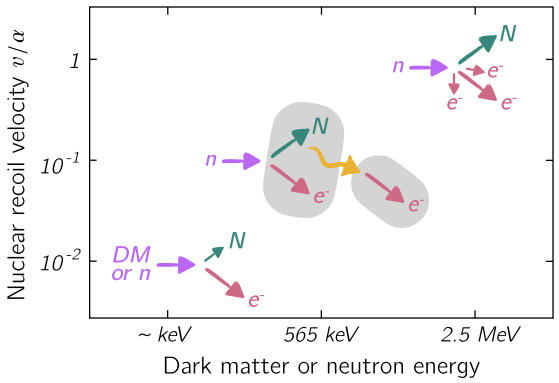

FIG. 1. Schematic representation of the different regimes for DM- and neutron-induced Migdal processes. The dimensionless quantity v/α is the nuclear recoil velocity relative to the fine-structure constant ($c = 1$). Bottom left: DM and low-energy neutron scattering, where the recoiling ion (N) is represented with a short arrow since its energy often falls below the detection threshold. Center: Midenergy neutron scattering in high-pressure gas can induce a distinctive two-cluster topology. The recoiling ion and the electron ionized through the Migdal effect induce one cluster, while the x ray emitted following de-excitation of the recoiling ion induces a second cluster, separated by several cm. Top right: High-energy neutron scattering from D-D/D-T fusion generators typically produces one hard and multiple soft ionization electrons, as represented by one longer and multiple shorter electron arrows.

The purposes of this article are threefold. Firstly, given the increasing interest in the Migdal effect for DM searches, and given that there is the potential for upcoming experiments to use this effect for DM discovery [51], precise predictions are needed for the low-energy regime probed by DM experiments. The previous state-of-the-art calculations appeared in Ref. [10] and used a relativistic self-consistent mean-field approach with the approximation of a local central potential [52]. We provide two additional, independent calculations of the Migdal effect. The first uses the GRASP [53–55] and RATIP [56] codes to calculate the bound and continuum wave functions, respectively. The second uses the BERTHA [57] code, and serves primarily as a cross-check of our results. Both approaches employ the canonical Dirac-Hartree-Fock method, and include the full nonlocal exchange potential in place of the empirical local potential employed in [10,52].

Secondly, the calculation of the Migdal effect in Ref. [10] assumed the dipole approximation. While this is a good approximation in the regime $v \ll \alpha$ characteristic of DM experiments, it is expected to fail at the higher values of v/α that can be probed in neutron scattering. We therefore calculate the Migdal transition probabilities without making this approximation, instead evaluating the multielectron matrix elements. Furthermore, we provide a detailed characterization of the regime of validity of the dipole approximation.

Thirdly, multiple electrons can be ionized through the Migdal effect in the regime where $v \simeq \alpha$ [58–64], and so we calculate the probability of double ionization events in neutron-beam experiments, as well as in DM scattering. We also introduce the 'semi-inclusive' probability to produce a hard electron in addition to one or more soft electrons (which would be below typical experimental thresholds and therefore not observable). We find that this semi-inclusive rate is needed to obtain accurate predictions for high-energy neutron-beam experiments; this is due to the importance of multiple ionization, which causes the semi-inclusive rate to grow with the energy of the recoiling nucleus.

We present results for the noble elements from helium to xenon, as well as for carbon, silicon, germanium and fluorine. The noble elements are widely used in DM scattering experiments, with CYGNUS planning to operate with gaseous He [65,66], NEWS-G with gaseous He and Ne [67–69], while Darkside [70] and DEAP-3600 [71] operate with liquid Ar, and LZ [72], PANDA-X [73], XENONnT [74], and the proposed XLZD [51,75] experiment use liquid Xe. The MIGDAL experiment [48] plans to operate with C and F in the form of low-pressure CF_4 gas, as well as CF_4 mixed with other gases including the noble elements, Si, and Ge.[3] The Migdal transition probabilities we have calculated are publicly available [77] for use by the community.

[3]A number of DM experiments use Si and Ge *semiconductor* detectors; the relevant formalism for the Migdal effect in semiconductors has been derived in [16,21,76].

The paper is organized as follows. In Sec. II we discuss the evaluation of the Migdal matrix element and introduce the semi-inclusive transition probability. In Sec. III we present our numerical results in the context of select illustrative examples. Section IV applies our results to DM and neutron-scattering experiments, and we conclude in Sec. V. Several appendixes contain details pertinent to our calculations.

II. MIGDAL PROBABILITY: GENERALITIES

There are several derivations of the Migdal effect in the literature [7,10,78], all of which converge on the same result (discussion on this point can be found in [79]). The most straightforward and intuitive way to derive the transition matrix element for an N-electron atom is through an argument due to A. Migdal [7,9]. In the rest frame of the nucleus it is the electron cloud that is boosted due to the nuclear recoil. Final-state electronic wave functions in this frame are therefore obtained by applying a Galilean boost to the electronic wave functions of the atom at rest. The required matrix element is then given by

$$\left\langle \Psi_f \left| \exp\left(i m_e \boldsymbol{v} \cdot \sum_{k=1}^{N} \boldsymbol{r}_k \right) \right| \Psi_i \right\rangle, \tag{1}$$

where m_e is the electron mass, $\boldsymbol{v}$ is the nuclear recoil velocity, and the sum is over the position operators $\boldsymbol{r}_k$ of the N electrons. The initial and final state electronic wave functions of the atom in the $v = 0$ frame are denoted by Ψ_i and Ψ_f, respectively.

Although the above argument relies on the sudden/impulse approximation (the assumption that the projectile-nucleus interaction timescale is short with respect to the electronic response time), the matrix element in Eq. (1) holds in general, up to corrections of $\mathcal{O}(m_e/m_{\mathrm{N}})$. If the interaction with the nucleus is long range, as in the case of dark matter scattering via a light mediator, then there is an additional form factor $F(q) \sim 1/q^2$. The situation is more complicated if the projectile interacts with electrons, in which case there will be an atomic form factor [58]. While neutrons interact with electrons via a magnetic dipole interaction, this effect is estimated to be negligible [9,61].

A. Exclusive transition probability

We first consider the probability to transition to a specific final state, which we term the *exclusive* transition probability. The matrix element in Eq. (1) contains an N-electron operator. As was pointed out in Ref. [61] in the context of closed-shell atoms, this can be rewritten in terms of single-electron matrix elements when the initial and final state wavefunctions are expressed as anti-symmetric products of single-electron wave functions. We denote the initial and final states by

$$\begin{aligned} |\Psi_i\rangle &= |\psi_{a_1}\psi_{a_2}\ldots\psi_{a_N}\rangle, \\ |\Psi_f\rangle &= |\chi_{b_1}\chi_{b_2}\cdots\chi_{b_N}\rangle, \end{aligned} \tag{2}$$

where $\{|\psi_a\rangle\}$ and $\{|\chi_b\rangle\}$ are two orthonormal bases of four-spinor single-electron wave functions from which the initial and final wave functions are constructed, respectively. The subscripts a_i and b_i denote the set of quantum numbers that describe the wave function; for relativistic bound states these are n_i (E_i for continuum states), κ_i, and m_i (see Appendix A 1). The transition matrix element for the Migdal effect then simplifies to

$$\langle \Psi_f | e^{i m_e \boldsymbol{v}\cdot\sum_k \boldsymbol{r}_k} | \Psi_i \rangle = \det(M), \tag{3}$$

with the $N \times N$ matrix of single-electron matrix elements

$$M_{\beta\alpha} = \langle \chi_{b_\beta} | e^{i m_e \boldsymbol{v}\cdot\boldsymbol{r}} | \psi_{a_\alpha} \rangle. \tag{4}$$

Following the standard approach, we evaluate these matrix elements by expanding the exponential operator in spherical tensors, as discussed in detail in Appendix A 1.

The exclusive transition probability is then

$$p_v(|\Psi_i\rangle \to |\Psi_f\rangle) = \det(MM^\dagger). \tag{5}$$

In practice, the relevant initial state is the atomic ground state, with $|\psi_{a_\alpha}\rangle$ the occupied orbitals in the ground state. On the other hand, for excitation (ionization) processes $|\Psi_f\rangle$ will include one or more excited (continuum) orbitals.

In this section we have, for clarity of presentation, considered the case where the atomic wave function can be expressed as a single Slater determinant. However, eigenstates of the atomic Hamiltonian are more accurately represented by configuration state functions (CSFs), which are linear combinations of Slater determinants. The generalization of Eqs. (3) and (5) to this case is provided in Appendix A 2.

B. Semi-inclusive transition probability

The probability for multiple ionization becomes significant when the recoil velocity $v \gtrsim \alpha$, as we shall see in explicit examples in Sec. III. However, for atoms with more than a handful of electrons, the large number of possible final states makes it impractical to calculate all of the exclusive transition probabilities. This motivates us to introduce the *semi-inclusive* probability $p_v(|\Psi_i\rangle \to |\chi_{b_1} X_{\mathrm{soft}}\rangle)$, which includes all final states with an electron in the state $|\chi_{b_1}\rangle$ and the remaining electrons, denoted collectively by X_{soft}, in either bound or continuum states with energies below some threshold E_{th}.

The semi-inclusive rate is of particular relevance for experiments aiming to observe the Migdal effect in neutron scattering. This is because the differential probability falls rapidly with increasing ionization electron energy; hence,

in an experiment where the electron energy threshold is $E_{\rm th} \sim \mathcal{O}(\text{keV})$, the expected signal is one hard electron with additional subthreshold excited or ionization electrons.

The semi-inclusive transition probability is

$$p_v(|\Psi_i\rangle \to |\chi_{b_1} X_{\rm soft}\rangle) = \frac{1}{(N-1)!} \sum_{b_2,\ldots,b_N}^{(E<E_{\rm th})} |\langle \chi_{b_1} \cdots \chi_{b_N} | e^{i m_e \boldsymbol{v}\cdot \sum_k \boldsymbol{r}_k} | \Psi_i \rangle|^2, \quad (6)$$

where the sum is over all states where $N-1$ electrons have energy less than $E_{\rm th}$ (here and in the following, the sum should be understood to include both the sum over bound orbitals and the integral over continuum orbitals). For $N > 2$ it is impractical to directly evaluate this expression but, given that the probability of producing multiple electrons above an $\mathcal{O}(\text{keV})$ threshold is negligible (justified below), a good approximation to the semi-inclusive probability is obtained by replacing $\sum_{b_2,\ldots,b_N}^{(E<E_{\rm th})} \to \sum_{b_2,\ldots,b_N}^{\text{all states}}$. In other words, the semi-inclusive probability is approximately equal to the probability of producing one hard electron with additional hard or soft electrons, $p_v(|\Psi_i\rangle \to |\chi_{b_1} X_{\rm soft}\rangle) \approx p_v(|\Psi_i\rangle \to |\chi_{b_1} X_{\rm all}\rangle)$. This leads to

$$\begin{aligned} p_v(|\Psi_i\rangle \to |\chi_{b_1} X_{\rm soft}\rangle) &\approx \langle \Psi_i | e^{-i m_e \boldsymbol{v}\cdot \sum_k \boldsymbol{r}_k} \left(\frac{1}{(N-1)!} \sum_{b_2,\ldots,b_N}^{\text{all states}} |\chi_{b_1} \cdots \chi_{b_N}\rangle\langle \chi_{b_1} \cdots \chi_{b_N}| \right) e^{i m_e \boldsymbol{v}\cdot \sum_k \boldsymbol{r}_k} |\Psi_i\rangle \\ &= \sum_{\alpha=1}^{N} |\langle \chi_{b_1} | e^{i m_e \boldsymbol{v}\cdot \boldsymbol{r}} | \psi_{a_\alpha} \rangle|^2, \end{aligned} \quad (7)$$

where the final result contains only single-electron matrix elements, with the sum over the occupied orbitals in the initial state. In going from the first to the second line of Eq. (7) we have used the orthogonality and completeness of the $\{|\chi_b\rangle\}$.

In deriving Eq. (7), we assumed that the probability of producing multiple electrons above threshold is negligible. We verify this numerically for several atoms in Sec. III, but it is expected to be true in general for sufficiently large $E_{\rm th}$. This is because the high-energy continuum radial wave functions oscillate rapidly, with wave number $\sim\sqrt{2 m_e E_e}$, which suppresses the radial integral with the initial-state bound electrons in the single-electron matrix elements [see Eq. (A6)]. However, this suppression disappears at high recoil velocities where the spherical Bessel function $j_L(m_e v r)$ in the integral oscillates with a comparable wave number. We therefore expect the approximation in Eq. (7) to eventually break down when $v \gtrsim \sqrt{2E_{\rm th}/m_e}$ and the probability for multiple hard emission becomes significant. For a typical experimental threshold, this corresponds to $v/\alpha \gtrsim 8.6\sqrt{(E_{\rm th}/1\ \text{keV})}$, which is larger than the maximum recoil velocity with a D-T neutron source (where the neutron energy is $\sim$14 MeV) for every element except helium. We have confirmed numerically for helium that this expression provides an excellent estimate for $\sim$keV thresholds.

Note that the above derivation can also be straightforwardly extended to obtain, for example, the two electron semi-inclusive rate $p(|\Psi_i\rangle \to |\chi_{b_1}\chi_{b_2} X_{\rm soft}\rangle)$. However, this is unlikely to be of practical relevance due to the very low probability of producing two high-energy ionization electrons. The generalization of Eq. (7) to open-shell systems is provided in Appendix A 2.

C. Dipole approximation

Most previous works have evaluated the matrix element in Eq. (1) using the dipole approximation, where the exponential is expanded to first order in v,

$$\exp\left(i m_e \boldsymbol{v} \cdot \sum_{k=1}^{N} \boldsymbol{r}_k \right) \approx 1 + i m_e \boldsymbol{v} \cdot \sum_{k=1}^{N} \boldsymbol{r}_k + \ldots. \quad (8)$$

It is important to establish the regime of validity of this approximation. A simple estimate uses the fact that atomic wave functions have support on distances of order the Bohr radius, a_0; the relevant expansion parameter is then $m_e v a_0 = v/\alpha$. It has previously been argued [18] that for ionization from inner shells a_0 should be replaced by the effective Bohr radius a_0/Z_n, where Z_n is the effective nuclear charge for the given shell. However, for the exclusive single ionization rate, this argument is incorrect. There is an additional subtlety, which is that the dominant correction to the dipole approximation comes not from the bound-continuum matrix element, but from outer shell bound-bound matrix elements appearing in the determinant of Eq. (4).

The breakdown of the dipole approximation can be understood using hydrogenic wave functions. The leading correction comes from the $ns \to np$ matrix element, which at leading order in v is proportional to $vn^2/(\alpha Z_n)$ [80]. The dipole approximation is therefore expected to be valid only when $v \ll \alpha Z_n/n^2$, where n should be taken as the principal quantum number of the valence shell. This means that the dipole approximation generally fails at lower v for larger atoms. While the above argument relies on hydrogenic wave functions, the same behavior is found in our numerical results, as we discuss in Sec. III C.

Interestingly, the dipole expansion provides a much better approximation to the semi-inclusive rate. This is because the latter depends only on the bound-continuum matrix elements in Eq. (7) and, for sufficiently high $E_{\rm th}$, inner shell ionizations provide the dominant contribution. The dipole approximation to Eq. (7) therefore holds when $v \ll Z_n/(m_e a_0) = \alpha Z_n$, where Z_n here denotes the effective charge for the shell that gives the largest contribution. It is interesting that despite the dipole operator only allowing for single electron transitions, it provides a good approximation to the *semi-inclusive* probability, including multiple ionization, up to corrections of order $(v/(\alpha Z_n))^2$.

III. MIGDAL PROBABILITY: NUMERICAL RESULTS AND ILLUSTRATIVE EXAMPLES

The previous section provided a general discussion of the Migdal effect and the methods for calculating transition probabilities when atomic wavefunctions are expressed as anti-symmetric products of single-electron wave functions. In this section, we describe our implementations of the general theory, and discuss select examples to illustrate particularly interesting aspects of our results.

We calculate the atomic wave functions with two independent implementations of the canonical Dirac-Hartree-Fock (DHF) formalism (for a recent review, see Ref. [81]), which use either basis-set or finite-difference methods for the radial functions. The basis-set approach, as implemented in the BERTHA [57] package, is ideally suited for the calculation of integrated probabilities, since the sum over states approaches completeness in a systematic way as the size of the basis set is increased. For the calculation of differential ionization probabilities we use the GRASP [53–55] and RATIP [56] packages to calculate the bound and continuum wave functions, respectively. Further details of our atomic calculations are provided in Appendixes A 3 and A 4. The use of two completely independent implementations also allows for important cross-checks of our results, and we find excellent agreement between the two approaches. The outputs from our numerical calculations are tables of transition probabilities, which we utilize in the subsequent discussion, and are made available for use by the community [77].

A. Integrated transition probabilities

We begin by discussing the integrated transition probabilities for helium and neon, as plotted in Fig. 2 as a function of the nuclear recoil velocity. These atoms cleanly illustrate many of the general features seen in larger atoms. Helium and neon are also of interest as proposed target gases for both the NEWS-G direct DM and MIGDAL neutron-scattering experiments.

In the upper panel of Fig. 2, the solid lines show the ground state-to-ground state (green, p_v^0), single transition (cyan, p_v^1) and double transition (purple, p_v^2) probabilities,

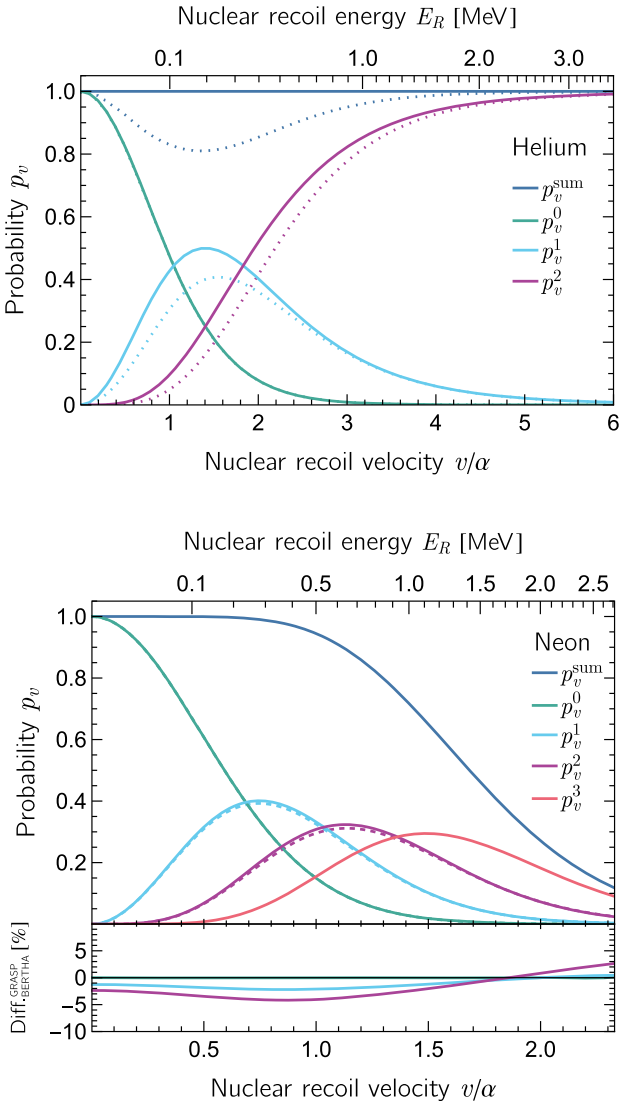

FIG. 2. Integrated transition probabilities as a function of nuclear recoil velocity for helium (upper) and neon (lower). The solid lines show the probability for no electronic transition p_v^0, single transition p_v^1, double transition p_v^2, and, for neon, triple transition p_v^3. Upper panel: The dotted lines correspond to single (cyan) and double (purple) ionization (i.e. transitions without bound excitations). Lower panel: The solid lines were calculated using BERTHA and the dashed ones with GRASP/RATIP. The lower subpanel shows the difference between them, $100 \times (p_v^{\rm GRASP}/p_v^{\rm BERTHA} - 1)$.

and their sum (dark blue, $p_v^{\rm sum}$). These include all possible transitions to bound-excited-orbitals or ionized continuum states, integrated over electron energies. For low nuclear recoil velocities, the most probable outcome is that the entire atom recoils, remaining in the electronic ground state; on the other hand, for sufficiently high-velocity recoils the atom is always fully ionized. In the special case of helium, all of the above quantities can be expressed purely in terms of ground-state matrix elements, using the

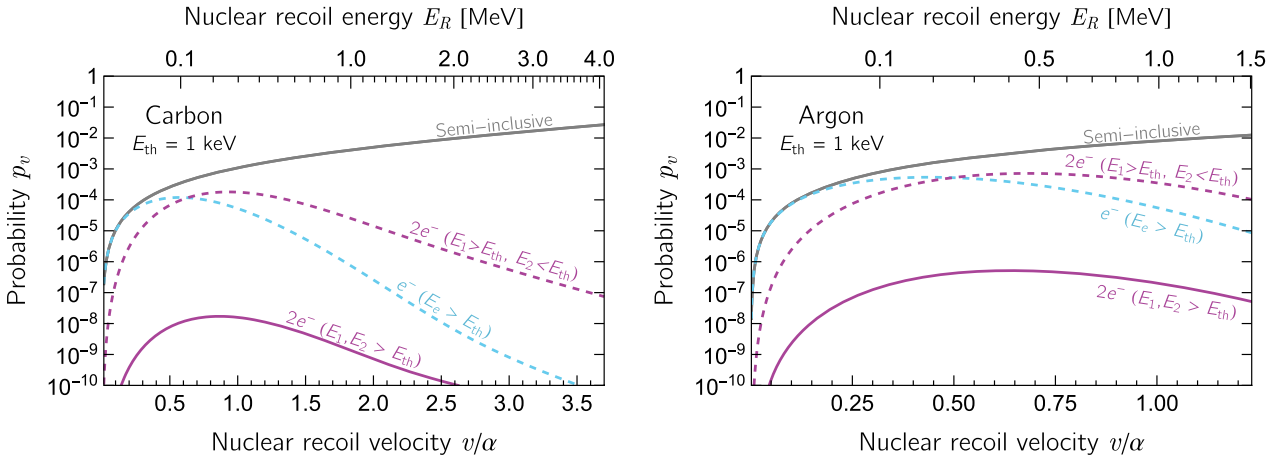

FIG. 3. Semi-inclusive ionization probabilities with $E_{\rm th} = 1$ keV as a function of nuclear recoil velocity (solid gray). The dashed cyan and purple curves show the contributions from exclusive single and double transitions, respectively. The solid purple line shows the probability for double ionization with both electron energies above 1 keV. The panels are for carbon (left) and argon (right).

completeness of the single electron wave functions and conservation of probability. Our implementations with BERTHA and GRASP/RATIP give near identical results for these matrix elements.

The dotted lines in the Fig. 2 upper panel show the probabilities for single ionization (cyan) and double ionization (purple) calculated with GRASP/RATIP; the dark blue-dotted line shows the sum of the ionization probabilities and p_v^0. From the difference between the ionization-only and single/double transition (solid) curves we see that, in helium, the final states with excited bound electrons contribute at most 20% of the total probability, and are completely negligible at high recoil velocities.

In the lower panel of Fig. 2 we show similar results for neon. Here, the solid lines were obtained using BERTHA and we include up to triple transitions. The neon calculation illustrates an important general feature for many-electron atoms, which is the significant probability for multiple ionization with increasing recoil velocity. We have not calculated quadruple and higher transitions, since it is computationally intensive, but it is clear that these become important in neon when $v \gtrsim \alpha$ and $p_v^{\rm sum} = p_v^0 + p_v^1 + p_v^2 + p_v^3$ (dark blue curve) falls significantly below one. Ultimately, for nuclear recoil velocities exceeding the orbital velocity of the inner shell electrons we expect the nucleus to effectively leave the entire electron cloud behind, leading to the complete ionization of the atom. For neon this corresponds to a velocity of $v \gtrsim 10\alpha$ or a recoil energy of around 50 MeV; recalling that the binding energy per nucleon is around 8 MeV for neon, it seems unlikely that the complete ionization of the atom from the Migdal effect would be achievable in practice.

The fact that $p_v^{\rm sum} = 1$ to a high accuracy at low recoil velocities, where quadruple and higher transitions are negligible, provides a strong consistency check of our results. A further cross-check is provided by our two separate implementations, with the lower subpanel of Fig. 2) showing the percentage difference between our two calculations ($p_v^{\rm GRASP}/p_v^{\rm BERTHA} - 1$). For ground-ground transitions the agreement is nearly perfect, and for single transitions the calculations agree within 2%. For double transitions the agreement has greater dependence on the recoil velocity, but is never worse than 5%.[4] The reason that the GRASP/RATIP calculation yields slightly lower probabilities is that it includes only a subset of the transitions to excited bound states[5]; BERTHA, on the other hand, does not distinguish between bound and continuum states, and the basis-set set we have used is sufficiently large to achieve good convergence.

B. Transition probabilities in the presence of an energy threshold

Although the probability of multiple ionization increases with the nuclear recoil velocity, the additional final-state electrons would only be observed by experiments with a very low electron energy threshold. The reason for this can be seen in Fig. 3, which shows the probabilities for double transitions in carbon (left) and argon (right) that yields either one (dashed purple line) or two (solid purple line) electrons with energies higher than 1 keV. The probability of obtaining two hard electrons is orders of magnitude smaller than having a single hard-electron across the whole range of nuclear recoil velocities, which extend to the

[4]We also compared our results for neon with Ref. [61], finding good agreement for $v/\alpha < 0.8$. At higher recoil velocities, Ref. [61] obtains larger single and double transition probabilities than both of our calculations (which are in close agreement).

[5]For neon, we have included orbitals up to $8s, 8p, 6d$; note that the excited bound orbitals from GRASP are also not strictly orthogonal to the continuum states from RATIP, as discussed in Appendix A 3.

maximum velocity induced by D-T neutron scattering. Accordingly, it is unlikely that Migdal events with multiple energetic electrons will be observed in either neutron-beam or DM experiments.[6]

The more relevant quantity for experiments is, therefore, the semi-inclusive probability to produce one ionization electron above threshold, with additional bound excitations or subthreshold ionization electrons. This is shown by the solid gray line in Fig. 3 with a threshold of $E_{\rm th} = 1$ keV for carbon (left) and argon (right). The dashed cyan and purple curves show the contributions to the semi-inclusive probability from single and double transitions, respectively. The semi-inclusive and exclusive single ionization curves are closely matched at low recoil velocities, but for recoil velocities $v/\alpha \gtrsim 0.3$ double and higher transitions cannot be neglected and eventually dominate.

The upper panel of Fig. 4 shows the contributions from individual initial-state orbitals to the single ionization probability, as a function of the ionization electron energy E_e. Ionization from the valence shell provides the dominant contribution at low E_e, while high-energy electrons are more likely to be ionized from the inner shell. Relativistic effects are small for fluorine, and the $p_{1/2}$ and $p_{3/2}$ curves are the same up to a multiplicity factor of $2/3$.

The middle panel of Fig. 4 shows the contributions of transitions from particular pairs of initial-state orbitals to the double ionization probability. In this panel we focus on the scenario where one ionization electron is soft and below a threshold of $E_{\rm th} = 1$ keV; we integrate over the energy of the soft electron and show the differential probability as a function of the hard electron's energy. For clarity, we have combined the $2p_{1/2}$ and $2p_{3/2}$ contributions and use nonrelativistic notation. The combination of ionization from the inner shell together with the valence shell $(1s, 2p)$ provides the dominant contribution at these energies. This behavior is consistent with that observed for single ionization, where ionization from the $1s$ and $2p$ subshells dominates for hard and soft electrons, respectively.

Finally, the lower panel of Fig. 4 shows the individual contributions to the sum over orbitals in Eq. (7) for the semi-inclusive probability. Again, we see that the leading contribution is from the $1s$ matrix element. The qualitative behavior observed in Fig. 4 is the same for all of the atoms we have studied, and does not change significantly with the recoil velocity up to overall normalization.

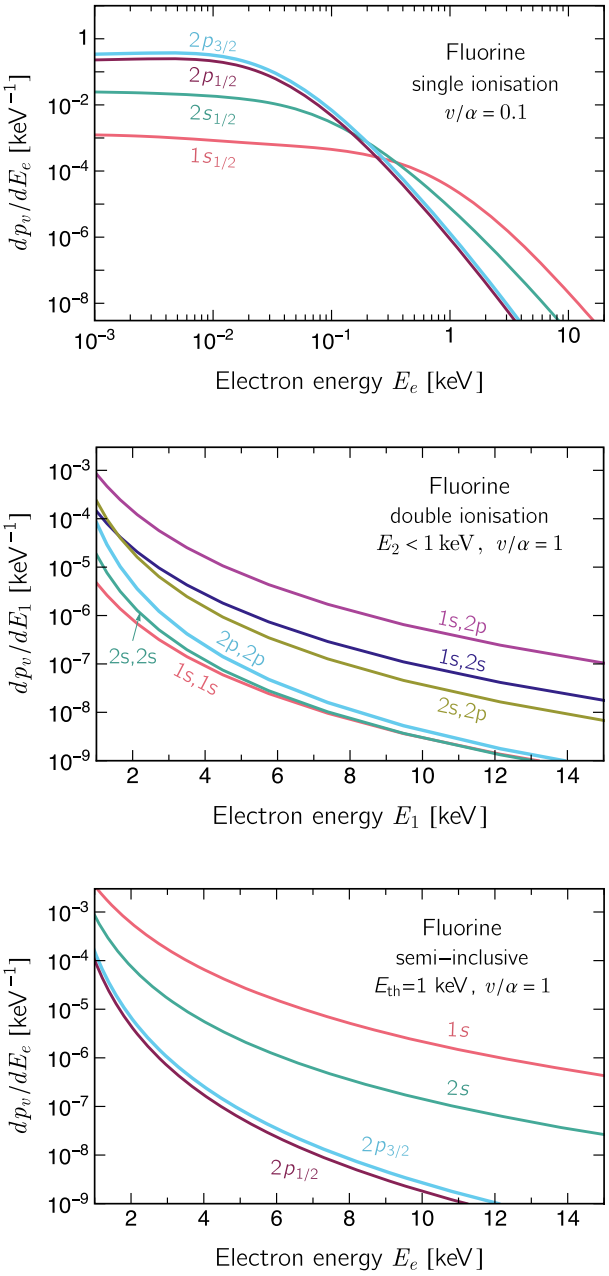

FIG. 4. Contributions to the differential ionization probability for fluorine from different initial-state orbitals. The upper panel is for single ionization; the middle panel shows double ionization when one ionization electron is soft ($E_2 < 1$ keV) while the other is hard ($E_1 > 1$ keV); and the lower panel shows the semi-inclusive probability. The upper and lower panels label the curves by the relativistic quantum numbers while, for clarity, the middle panel uses nonrelativistic notation.

C. Validity of the dipole approximation

In Fig. 5 we provide some examples that demonstrate the accuracy of the dipole approximation. First, in the upper panel we show the difference between the exclusive single ionization probability and the dipole approximation, $p_v^{\rm dipole}/p_v^{\rm single} - 1$. The solid and dashed curves show ionization from the $1s$ and valence subshells, respectively, of neon (blue) and xenon (red). As discussed in Sec. II C, and contrary to previous expectations in the literature, we see that the dipole approximation fails at roughly the same

[6]Ionization by the Migdal effect necessarily leads to atomic de-excitation, which may result in additional electrons through Auger (or Coster-Kronig) emission. For light atoms, the Auger electron will also be sub-keV. See Ref. [48] for further discussion.

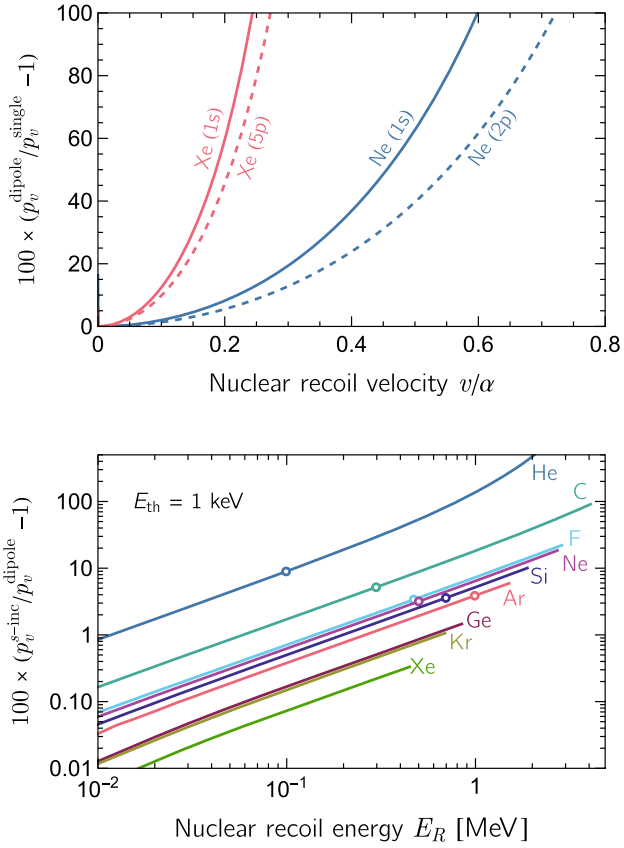

FIG. 5. Upper panel: Difference between the exclusive single ionization probabilities and the dipole approximation for the $1s$ and valence subshells of neon and xenon. Lower panel: Difference between the semi-inclusive ionization probability and the dipole approximation for various atoms. The open circles denote where $v = \alpha$.

recoil velocity for both subshells. In fact, it is only the valence subshell that behaves slightly differently and all other subshells closely follow the $1s$ curve. We also see that the dipole approximation breaks down at a lower recoil velocity for xenon than neon. More generally, we find that the dipole approximation provides a good approximation to the exclusive ionization probability only when $v \ll \alpha Z_n/n^2$, with n the principal quantum number of the valence shell, which is consistent with the expectations from Sec. II C.

The lower panel of Fig. 5 shows the difference between the semi-inclusive probability and the dipole approximation, $p_v^{\text{s-inc}}/p_v^{\text{dipole}} - 1$, as a function of the nuclear recoil energy for several different atoms. The endpoints of the curves correspond to the maximum nuclear recoil energy from incident D-T neutrons. Recall from section II C that the dipole result is expected to provide a good approximation to the semi-inclusive probability when $v \ll \alpha Z_n$. For helium, this corresponds to $E_R \ll 0.4$ MeV, which is entirely consistent with our numerical results in Fig. 5. For heavy atoms, such as xenon, we see that the dipole approximation should be sufficiently accurate for most cases of practical interest; however, this is clearly not the case for lighter atoms, where it significantly underestimates the semi-inclusive probability for large nuclear recoil energies.

IV. MIGDAL PHENOMENOLOGY

In this section we present two applications of our calculations. The first is to sub-GeV DM direct detection, where the nuclear recoil velocity is small, $v \ll \alpha$, and single ionization is the dominant process. The second is to neutron scattering, where we assume the neutrons originate from D-D or D-T fusion generators and the nuclear recoil velocity can satisfy $v \simeq \alpha$, so that multiple ionization dominates.

A. Dark matter

Consider DM that interacts with the nucleus via the usual spin-independent operator. The differential rate (per unit target mass) to produce a nuclear recoil with energy E_R and an ionization electron with energy E_e factorizes and can be cast in the form

$$\frac{d^2R}{dE_R dE_e} = \frac{\rho_\chi A^2 \sigma_n}{2 m_\chi \mu_{\chi n}^2} |F_{\rm N}|^2 \sum_{n\kappa} \frac{dp_v(n\kappa \to E_e)}{dE_e} g_\chi(v_{\rm min}), \quad (9)$$

where the local DM density is $\rho_\chi \simeq 0.3\ \text{GeV cm}^{-3}$, m_χ is the DM mass, A the atomic mass number of the target, $\mu_{\chi n}$ the DM-nucleon reduced mass, σ_n the spin-independent DM-nucleon scattering cross-section at zero-momentum transfer, and for $F_{\rm N}$ we use the Helm nuclear form factor [82]. The probability to ionize an electron with initial quantum numbers (n, κ) into a final state with kinetic energy E_e is $p_v(n\kappa \to E_e)$. Finally, the standard integral over the DM velocity distribution is

$$g_\chi(v_{\rm min}) = \int_{v_{\rm min}}^{\infty} \frac{f_\chi(\vec{v}_\chi + \vec{v}_\oplus)}{|\vec{v}_\chi|} d^3\vec{v}_\chi, \quad (10)$$

where $f_\chi(\vec{v}_\chi)$ is taken to be a truncated Maxwell-Boltzmann distribution and we follow the recommendations in Ref. [83] and set $v_0 = \sqrt{2}\sigma_v = 238\ \text{km s}^{-1}$ and $v_{\rm escape} = 544\ \text{km s}^{-1}$. We neglect the time dependence of $\vec{v}_\oplus$, the motion of the Earth with respect to the galactic rest frame [84]. The minimum velocity of DM that can inelastically scatter to produce a nuclear recoil with energy E_R and an electronic excitation of energy $E_{\rm EM}$ is

$$v_{\rm min} = \sqrt{\frac{m_{\rm N} E_{\rm R}}{2\mu^2}} + \frac{E_{\rm EM}}{\sqrt{2 m_{\rm N} E_{\rm R}}}, \quad (11)$$

where $m_{\rm N}$ is the nucleus mass and $E_{\rm EM} = E_e + E_{n\kappa}$, with $E_{n\kappa}$ the (positive) binding energy of the electron before

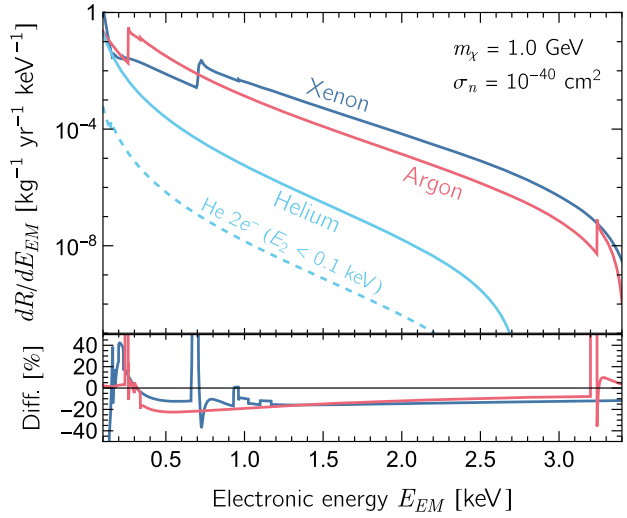

FIG. 6. Differential DM scattering rate (per unit target mass) as a function of the total electronic energy for helium, argon and xenon targets, with a DM-nucleon spin-independent cross section of $\sigma_n = 10^{-40}$ cm^2 and a DM mass of 1 GeV. The lower panel shows the difference between our result and the rate obtained using the dipole approximation for $dp_v/dE_{\rm EM}$ from Ref. [10], $(dR/dE_{\rm EM})_{\rm dipole}/(dR/dE_{\rm EM}) - 1$. The cyan dashed line shows the rate of double transitions in helium, where we integrated over the energy of the second, soft electron up to 0.1 keV.

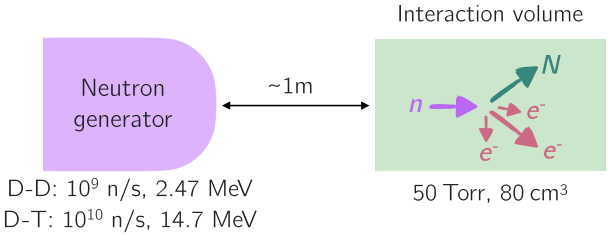

FIG. 7. Schematic representation of the MIGDAL experiment. The D-D (D-T) generator emits mono-energetic neutrons at 2.47 (14.7) MeV and approximately isotropically at an intensity of 10^9 (10^{10}) neutrons per second. Neutrons scatter in the interaction volume contained within an OTPC, which images nuclear and electron ionization tracks. Long and short electron arrows represent one hard ionization electron and additional subthreshold electrons, the dominant Migdal process for these generators.

emission. Note that since $v_{\rm min}$ depends on (n, κ) through $E_{n\kappa}$, $g_\chi(v_{\rm min})$ should be included in the sum in Eq. (9). For multiple ionization, $E_{\rm EM}$ is modified to include the sum of the binding energies of each of the electrons.

In Fig. 6 we show the differential DM scattering rate as a function of the total electronic energy, $E_{\rm EM}$, for helium, argon and xenon. Results for He, relevant for the CYGNUS and NEWS-G experiments, have not been presented in the literature before. We have assumed a DM mass of 1 GeV and a DM-nucleon scattering cross section of 10^{-40} cm^2. For argon (xenon), one can clearly identify the thresholds where ionization from the $n = 2$, 1 ($n = 3$) shells becomes kinematically accessible. The dashed line shows the rate of double transitions in helium, including both double ionization and ionization with excitation, where the second electron is soft ($E_2 < 0.1$ keV). As expected, the double transition rate is highly suppressed due to the low nuclear recoil velocity ($v/\alpha \lesssim 0.1$) induced by the scattering DM.

The dipole approximation is expected to be valid in the kinematic regime relevant for DM scattering. In the bottom subpanel of Fig. 6 we compare (for Ar and Xe) the rate obtained with our transition probabilities to the dipole approximation results of Ref. [10], $(dR/dE_{\rm EM})_{\rm dipole}/(dR/dE_{\rm EM}) - 1$. We indeed find good agreement between the two calculations, verifying existing DM limits based on the Migdal effect. In fact, the differences are primarily due to the differing calculations of the atomic wave functions, rather than the use of the dipole approximation. Specifically, we use the local DHF exchange potential in contrast to the effective central potential approximation employed in Ref. [10]. In Fig. 6 we have used the theoretical values for the orbital binding energies in $E_{\rm EM}$, which differ between the two calculations. This is the source of the larger differences near thresholds. We provide further comparisons of our ionization probabilities with the dipole results of Ref. [10] in Appendix B.

B. Neutron scattering

There are several experimental proposals to test the theory underlying the Migdal effect with neutron sources. These experiments will probe an energy regime above that being exploited by DM experiments, but the systematic study of the Migdal effect in various atomic species will test theoretical predictions of the Migdal effect over a wide energy regime. We focus on the phenomenology relevant to the MIGDAL experiment since it uses the highest-energy neutron sources and results in phenomenology that is most distinct from DM scattering—and was one of the key motivations for the present work.

A schematic representation of the MIGDAL experiment is shown in Fig. 7. The experiment will operate with intense neutron beams from D-D and D-T fusion generators, which are directed towards an optical time-projection chamber (OTPC) situated 1 meter away for the D-T generator and 0.5 meters away for the D-D generator.[7] The OTPC will be filled with low-pressure gas; initially pure CF_4 and later CF_4-based mixtures with noble elements or Si or Ge compounds. Nuclear and electron recoils within the low-pressure gas result in ionization tracks. The telltale sign of a Migdal event is a nuclear recoil track and an electron ionization track emerging from a common vertex. The ionization tracks must be sufficiently long to discriminate

[7]We ignore the mild dependence of the neutron intensity on the orientation of the generator and assume that the neutrons are emitted isotropically. We use the neutron energies for the generator orientations that will be used by the MIGDAL experiment.

between electron and nuclear recoils; at a pressure of 50 Torr, this implies an electron energy threshold of approximately 5 keV and a nuclear recoil threshold of around 150 keV [48].

The rate for neutron-induced Migdal events in a gas mixture again factorizes and can be expressed as

$$\frac{d^2R}{dE_R dE_e} = \phi_n \sum_i N_T^i \frac{d\sigma_s^i}{dE_R} \sum_{n\kappa} \frac{dp_v^i(n\kappa \to E_e)}{dE_e}, \qquad (12)$$

where ϕ_n is the neutron flux, the sum over i runs over all species in the gas mixture (e.g., $i = \{\mathrm{C}, \mathrm{F}, \mathrm{Ar}\}$ in a CF_4 + Ar mixture), and N_T^i, σ_s^i, and $p_v^i(n\kappa \to E_e)$ are the number of target atoms in the interaction volume, the neutron-nucleus cross section, and the transition probability for the ith atomic species, respectively. The number of target atoms is calculated assuming the gas is at ambient temperature (293.15 K) and the interaction volume is 80 cm^3 so that, for instance, CF_4 gas at 50 Torr contains 1.3×10^{20} molecules. To calculate N_T^i, we treat each CF_4 molecule as one carbon atom and four fluorine atoms.

An important difference with respect to DM scattering is that the neutron has sufficient energy to excite the nucleus. Immediately after the scattering, the excited nucleus is moving with respect to the electron cloud and so can still lead to electron emission through the Migdal effect. Therefore, σ_s should include the contributions from all reactions that result in the topology in Fig. 7: elastic scattering, inelastic scattering, $(n, 2n)$ reactions and radiative capture reactions, since all produce bare nuclear recoils (i.e. without accompanying charged tracks) and the photon released during de-excitation of the nucleus escapes the low-pressure gas without interacting. Differential and integrated neutron-nucleus cross sections that we use in this work are given in Appendix C.

Treating the molecule as a sum of discrete atomic nuclei should be a very accurate approximation in the context of the neutron-nucleus interaction, since the de Broglie wavelength of the neutron at D-D or D-T energies is $\sim 10^{-14}$ m, which is orders of magnitude smaller than the C-F bond length. The approximation of using the atomic result for the transition probability, $p_v^i(n\kappa \to E_e)$, rather than performing a molecular calculation, requires a more careful justification. As a starting point, it has been shown that the general form of the transition matrix element, Eq. (1), remains the same for both atoms and molecules (up to corrections of order m_e/m_N) [78]. It is also common practice to model the molecular electronic wave functions in terms of antisymmetric products of single-electron wave functions (molecular orbitals). Taken together, this implies that the formalism in Sec. II extends to the case of molecules; this particularly applies to the derivation of the semi-inclusive rate where the only assumption made about the soft-electron wave functions is that they are orthogonal and complete, which holds for both atoms and molecules.

In the context of the MIGDAL experiment, we expect that the atomic result for the semi-inclusive transition probability will provide a good approximation to the molecular result. This is because the MIGDAL experiment employs an $\mathcal{O}(\mathrm{keV})$ energy threshold, so as Fig. 4 demonstrates, the transition probability is dominated by the core (innermost) electrons. This is important because, after molecular bonding, the core electrons in the CF_4 molecule are only slightly modified from their atomic forms. This is evidenced by the experimental values of the binding energies: the $1s$ binding energy in the fluorine atom is 697 eV [85], while the $1t_2/1a_1$ states in CF_4 (the core states equivalent to $1s$) have a binding energy of 695 eV [86]. We therefore expect that when the core electrons dominate the scattering rate, which is the case for the MIGDAL experiment, the atomic transition probability will provide a reasonable approximation to the full molecular result.

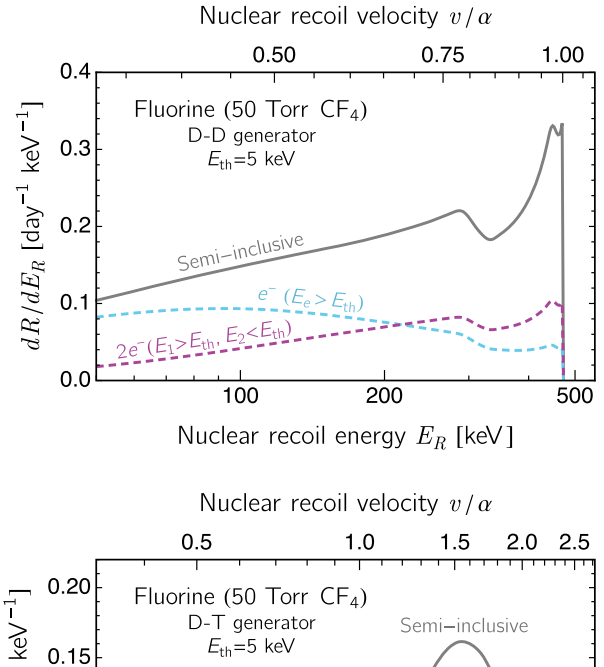

FIG. 8. Differential scattering rate as a function of the nuclear recoil energy for fluorine in CF_4 gas at 50 Torr from a D-D (top) and D-T (bottom) neutron generator. Electron energies above the threshold of $E_{th} = 5$ keV have been integrated over. The solid gray curve shows the semi-inclusive rate while the dashed cyan and purple curves show the contributions from single and double transitions, respectively.

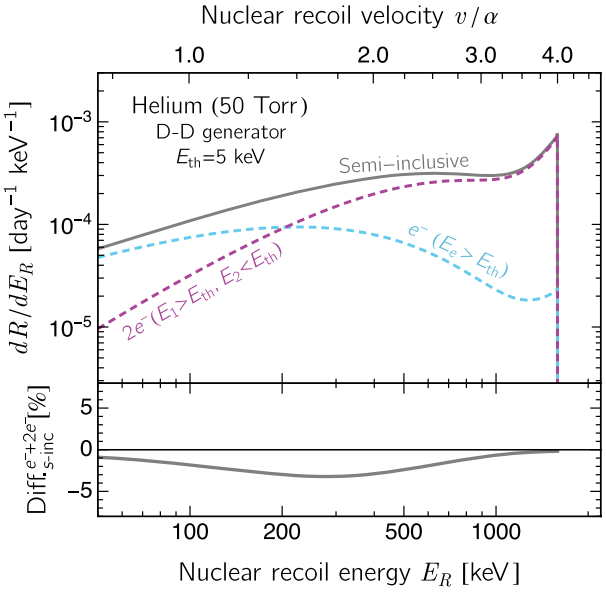

FIG. 9. Differential scattering rate as a function of the nuclear recoil energy for helium gas at 50 Torr from a D-D neutron generator. Electron energies above $E_{th} = 5$ keV have been integrated over. The solid gray curve shows the semi-inclusive rate while the dashed cyan and purple curves show the contributions from single and double transitions, respectively. The lower panel shows the percentage difference between the sum of the exclusive single and double transition rates and the semi-inclusive rate, $(dR/dE_R)_{e^-+2e^-}/(dR/dE_R)_{\text{s.-inc}} - 1$.

Further work is warranted to quantify the level of agreement but such a study lies beyond the scope of this work.

With the above assumptions, the result for the fluorine differential scattering rate with an electron energy threshold of $E_{th} = 5$ keV in CF_4 gas at 50 Torr is shown in the upper (lower) panel of Fig. 8 for the D-D (D-T) neutron generator. The dotted lines show the rate for single ionization (cyan) and double transitions (purple), while the solid gray line shows the semi-inclusive rate. In both cases the semi-inclusive curve matches the sum of the single and double rates at $v/\alpha \approx 0.3$. However for higher values of v/α, and most dramatically in the case of the D-T generator, the semi-inclusive rate departs significantly from the combined single and double rates. This behavior is consistent with that shown in Fig. 3 for the transition probabilities.

Helium provides an interesting example since we can directly compare the semi-inclusive calculation with the sum of the exclusive transitions. The differential scattering rate induced by a D-D generator directed at helium gas at 50 Torr is shown in Fig. 9.[8] The solid gray line again shows the semi-inclusive rate, while the dashed purple line shows the double transition rate. As expected, the single ionization rate dominates at low values of v/α, while the double transition rate dominates at larger values. The lower panel shows the percentage difference between the sum of exclusive transitions and the semi-inclusive rate, $(dR/dE_R)_{e^-+2e^-}/(dR/dE_R)_{\text{s.-inc}} - 1$. We find good agreement at the level of a few % or better across the whole nuclear recoil range; $(dR/dE_R)_{e^-+2e^-}$ slightly underestimates $dR/dE_R|_{\text{s.-inc}}$, with the small difference arising because the excited bound orbitals from GRASP and the continuum states from RATIP are not strictly orthogonal, as discussed in Appendix A 3, so the ionization with excitation rate is slightly underestimated.

[8]Experimentally, it may be more favorable to operate with helium gas at higher pressure [48], but for ease of comparison with other elements, we present results for 50 Torr.

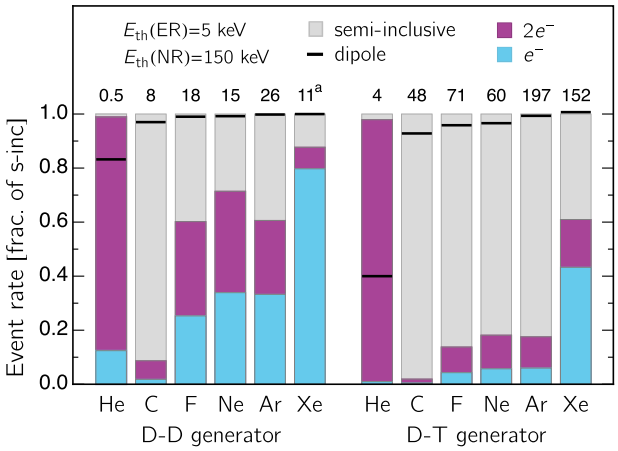

FIG. 10. Event rates for several atomic elements with D-D (left set of columns) and D-T (right set of columns) generators and electron and nuclear recoil energy thresholds of 5 keV and 150 keV, respectively. (For xenon with the D-D generator $E_{th}(\text{NR}) = 50$ keV.) The numbers above each column give the events-per-day for 50 Torr gas. The coloured columns show the stacked event rates for single (cyan) and double (purple) transitions relative to the semi-inclusive rate. The black line in each column shows the dipole approximation event rate relative to the semi-inclusive rate.

In Fig. 10, we compare the number of Migdal events induced by a D-D generator (left set of columns) and a D-T generator (right set of columns) in several single-species gas targets. The expected number of events per day is listed above the column for each element, assuming a gas pressure of 50 Torr and an experimental setup as in Fig. 7. These were obtained by integrating the semi-inclusive rate above an electron energy threshold of 5 keV and a nuclear recoil energy threshold of 150 keV. The only exception is for xenon with the D-D generator where the endpoint energy is approximately 75 keV, so we instead integrated over nuclear recoil energies above 50 keV. With both neutron generators, we see that there is the possibility of inducing tens or hundreds of Migdal events over a short data-taking period consisting of a few days.

The cyan columns in Fig. 10 show the single ionization event rate relative to the semi-inclusive rate. The purple

columns show the event-rate from double transitions,[9] again relative to the semi-inclusive rate, stacked above the single ionization contribution. For helium the single plus double transition rate (i.e. the total height of the cyan and purple columns) almost exactly matches the semi-inclusive rate, consistent with Fig. 9. However, for all of the other gases it underestimates the semi-inclusive rate. The discrepancy is largest for lighter atoms (helium excluded) and for the D-T generator where the nuclear recoils extend to larger values of v/α.

Finally, the black line in each column of Fig. 10 indicates the event-rate obtained using the dipole approximation, relative to the semi-inclusive rate. The general trend is consistent with that shown in Fig. 5; the dipole approximation provides a good approximation for the heavier atoms, while for lighter atoms it significantly underestimates the semi-inclusive rate, especially for the larger nuclear recoil energies induced by the D-T generator.

V. CONCLUSIONS

The excitation or emission of an electron after a sudden jolt to the atomic nucleus by an electrically-neutral projectile is known as the Migdal effect. In recent years, the Migdal effect has gained prominence in direct detection searches for sub-GeV DM, and there are now several proposals to measure the effect using neutron sources. The parameter that characterizes the probability of electron emission is v/α, the dimensionless ratio of the nuclear recoil velocity relative to the fine-structure constant multiplied by the speed of light. Previous studies have focused on the regime where $v/\alpha \ll 1$, which is most relevant for DM direct detection searches. We have advanced the theory underlying the Migdal effect in the $v \simeq \alpha$ regime, introducing the semi-inclusive probability that is essential for accurate predictions in fast neutron scattering.

We have undertaken two independent calculations of the Migdal effect, solving the Dirac-Hartree-Fock equations using the finite difference and basis-set methods as implemented in GRASP and BERTHA, respectively. We have calculated electron-transition probabilities for noble elements from helium to xenon, as well as for carbon, silicon, germanium and fluorine. In addition to calculating single ionization probabilities, which are in good agreement with previous calculations when $v/\alpha \ll 1$, we have undertaken calculations of multiple ionization. We have shown that multiple ionization dominates when $v \sim \alpha$, but that the probability of obtaining multiple electrons with energies above an $\mathcal{O}(\mathrm{keV})$ experimental threshold is extremely small. Accordingly, we have emphasized the importance of the *semi-inclusive* transition probability, which accounts for all processes that yield one hard electron, with any number of additional soft, subthreshold electrons. We have also clarified the role of the dipole approximation. While this approximation is only formally defined for single transitions, we have found that it, perhaps surprisingly, yields a good estimate of the semi-inclusive probability for all but the lightest atoms.

We have applied our results for the Migdal effect in the context of both DM direct detection and neutron scattering experiments. In the DM case, we found good agreement between our single ionization calculations and previous results. Furthermore, we confirmed that the double ionization rate is highly suppressed, owing to the low nuclear recoil velocities involved, and can be safely ignored. We have performed the first calculations of the Migdal effect in DM-helium scattering, which will enable experiments that use this element to increase their sensitivity to sub-GeV DM. For neutron scattering, we focused on the phenomenology relevant to the MIGDAL experiment, which employs D-D and D-T neutron generators. At the nuclear recoil velocities induced by these generators, we have shown that the multiple ionization rate is significant and cannot be ignored; it is imperative that the semi-inclusive probabilities are used to provide the most accurate description of the Migdal effect.

Our work has been carried out in the context of atomic systems. While we have argued that the atomic calculations should provide a good approximation for the core electrons in CF_4, a molecular gas that will be used in the MIGDAL experiment, work remains to extend the formalism so that it applies to all electrons in the molecular system. Similarly, we have ignored complications due to the electronic band structure in liquid noble elements, relevant for DM direct detection experiments. Further work is warranted to extend the theory to these systems. We hope to address some of these issues in the future.

Data Access Statement: The data supporting the findings reported in this paper are openly available from the GitHub repository at [77].

ACKNOWLEDGMENTS

P. C. is supported by the Australian Research Council Discovery Early Career Researcher Award No. DE210100446. M. J. D. is supported by the Australian Research Council. This work was supported by the Australian Research Council through the ARC Centre of Excellence for Dark Matter Particle Physics, CE200100008. C. M. is supported by the UKRI's Science and Technology Facilities Council (Awards No. ST/N004663/1, No. ST/V001876/1, and No. ST/T000759/1). We are grateful to members of the MIGDAL Collaboration for discussions and particularly thank T. Marley (Imperial) for generating the neutron scattering cross sections used in this work. For the purpose of open

[9]For all elements except xenon, this includes both double ionization and ionization with excitation, with the latter contributing ~5% to the double transition rate; only double ionization is included for xenon.

APPENDIX A: ATOMIC PHYSICS

1. Relativistic single-electron matrix elements

To evaluate the Migdal transition matrix element, we require single-electron matrix elements of the form

$$M^{n'\kappa'm'}_{n\kappa m} \equiv \langle n',\kappa',m'|\exp(im_e\boldsymbol{v}\cdot\boldsymbol{r})|n,\kappa,m\rangle, \quad \text{(A1)}$$

where $\langle \boldsymbol{r}|n,\kappa,m\rangle$ is a four-component atomic Dirac spinor that satisfies

$$\begin{aligned}\langle \boldsymbol{r}|h_D|n,\kappa,m\rangle &= \langle \boldsymbol{r}|\boldsymbol{\alpha}\cdot\boldsymbol{p}+\beta m_e + V(\boldsymbol{r})|n,\kappa,m\rangle \\ &= E_n\langle \boldsymbol{r}|n,\kappa,m\rangle, \end{aligned} \quad \text{(A2)}$$

with n denoting the principal quantum number, m the J_z quantum number, $V(\boldsymbol{r})$ the potential, and $\boldsymbol{\alpha}$ and β are the 4×4 Dirac matrices [87]. The quantum number κ is the eigenvalue of the operator $K=-1-\boldsymbol{\sigma}\cdot\boldsymbol{l}$ and can be written as

$$\kappa = \begin{cases} -(l+1) & j=l+1/2 \quad (\kappa<0) \\ +l & j=l-1/2 \quad (\kappa>0), \end{cases} \quad \text{(A3)}$$

with l and j the orbital and total angular momentum quantum numbers respectively. For continuum states the discrete label n is replaced with the continuous label E. We normalize our continuum spinors with respect to energy, $\int dE\langle\psi_{E',\kappa',m'}|\psi_{E,\kappa,m}\rangle=\delta(E-E')$.

The four-component spinors are separable in radial and spin-angular coordinates and can be written as (see e.g., [88])

$$\langle \boldsymbol{r}|n,\kappa,m\rangle = \frac{1}{r}\begin{pmatrix} P_{n,\kappa}(r)\chi_{\kappa,m}(\vartheta,\varphi) \\ iQ_{n,\kappa}(r)\chi_{-\kappa,m}(\vartheta,\varphi)\end{pmatrix}, \quad \text{(A4)}$$

where $P_{n,\kappa}(r)$ and $Q_{n,\kappa}(r)$ are, respectively, the large and small component radial functions and $\chi_{\pm\kappa,m}(\vartheta,\varphi)$ are two-component spin-angular functions.

As usual, the operator $\exp(im_e\boldsymbol{v}\cdot\boldsymbol{r})$ is written as the spherical tensor expansion

$$\exp(im_e\boldsymbol{v}\cdot\boldsymbol{r}) = 4\pi\sum_{L,M} i^L j_L(m_e v r)Y_L^{M*}(\hat{\boldsymbol{v}})Y_L^M(\hat{\boldsymbol{r}}), \quad \text{(A5)}$$

where $j_L(x)$ is the spherical Bessel function. The spin-angular parts of the matrix element are independent of $\mathrm{sgn}(\kappa)$ and $\mathrm{sgn}(\kappa')$, which allows us to write the matrix element in the form

$$\begin{aligned} M^{n'\kappa'm'}_{n\kappa m} &= \sqrt{4\pi}\sum_{L,M} i^L\sqrt{2L+1}Y_L^M(\hat{\boldsymbol{v}})d_M^L(j',m';j,m) \\ &\times\int_0^\infty dr\, j_L(m_e v r)[P_{n,\kappa}(r)P_{n',\kappa'}(r) \\ &+ Q_{n,\kappa}(r)Q_{n',\kappa'}(r)]. \end{aligned} \quad \text{(A6)}$$

The angular coefficients can be determined via the Wigner-Eckart theorem and are given by

$$\begin{aligned} d_M^L(j',m';j,m) &= (-1)^{2j'-m'+1/2}[j,j']^{1/2}\Pi^e(\kappa,\kappa';L) \\ &\times\begin{pmatrix} j' & L & j \\ -m' & M & m\end{pmatrix}\begin{pmatrix} j' & L & j \\ 1/2 & 0 & -1/2\end{pmatrix}, \end{aligned} \quad \text{(A7)}$$

where $[j,j']=(2j+1)(2j'+1)$, and $\Pi^e(\kappa,\kappa';L)$ implements the even-parity selection rule and is equal to one if $l+l'+L$ is even and zero otherwise. In practice, the limits on the sum over L in Eq. (A6) are determined by the selection rules of the $3j$ symbols that appear in Eq. (A7).

2. Transition probabilities with configuration state functions

As usual, we describe atomic wave functions with configuration state functions. These are linear combinations of Slater determinants that, in the relativistic case, are eigenfunctions of energy, the total angular momentum operators, $\boldsymbol{J}$ and J_z, and parity. In this appendix we generalize the results of Sec. II, which were derived for wave functions consisting of a single Slater determinant. We write the initial and final-state atomic wave functions as

$$\begin{aligned} |\Psi_i\rangle &= \sum_\gamma C_i^\gamma|\Psi_i^\gamma\rangle, \\ |\Psi_f\rangle &= \sum_\gamma C_f^\gamma|\Psi_f^\gamma\rangle, \end{aligned} \quad \text{(A8)}$$

with $|\Psi_i^\gamma\rangle=|\psi_{a(\gamma)_1}\ldots\psi_{a(\gamma)_N}\rangle$, $|\Psi_f^\gamma\rangle=|\chi_{b(\gamma)_1}\ldots\chi_{b(\gamma)_N}\rangle$ single-Slater-determinant wave functions and C_i^γ, C_f^γ constant coefficients.

a. Exclusive transition probability

Using the above expressions for the initial and final state wave functions, the generalization of the exclusive transition probability from Eq. (5) is

$$p_v(|\Psi_i\rangle\to|\Psi_f\rangle) = \left|\sum_{\gamma,\gamma'}(C_f^{\gamma'})^*C_i^\gamma\det(M^{\gamma'\gamma})\right|^2. \quad \text{(A9)}$$

As in Eq. (4), $M^{\gamma'\gamma}$ is an $N\times N$ matrix of single-electron matrix elements

$$(M^{\gamma'\gamma})_{\beta\alpha} = \langle\chi_{b(\gamma')_\beta}|\exp(im_e\boldsymbol{v}\cdot\boldsymbol{r})|\psi_{a(\gamma)_\alpha}\rangle, \quad \text{(A10)}$$

where $|\psi_{a(\gamma)_\alpha}\rangle$ and $|\chi_{b(\gamma')_\beta}\rangle$ are occupied orbitals in $|\Psi_i^\gamma\rangle$ and $|\Psi_f^{\gamma'}\rangle$, respectively.

b. Semi-inclusive transition probability

In Sec. II we defined the semi-inclusive transition probability, which includes all final states containing a single continuum electron with $E_e > E_{\rm th}$ and any number of additional subthreshold excitations. To perform the sum over final states it is more convenient to work in the determinant basis for the final states. The initial-state atomic wave function, on the other hand, is given by a particular linear combination of determinants, as in Eq. (A8). The semi-inclusive probability can then be written as

$$\begin{aligned} p_v(|\Psi_i\rangle \to |\chi_{b_1} X_{\rm soft}\rangle) &= \frac{1}{(N-1)!}\sum_{b_2,\ldots,b_N}^{(E<E_{\rm th})} |\langle \chi_{b_1}\cdots\chi_{b_N}|e^{im_e \boldsymbol{v}\cdot\sum_k \boldsymbol{r}_k}|\Psi_i\rangle|^2 \\ &\approx \langle\Psi_i|e^{-im_e \boldsymbol{v}\cdot\sum_k \boldsymbol{r}_k}\left(\frac{1}{(N-1)!}\sum_{b_2,\ldots,b_N}^{\text{all states}} |\chi_{b_1}\cdots\chi_{b_N}\rangle\langle\chi_{b_1}\cdots\chi_{b_N}|\right)e^{im_e \boldsymbol{v}\cdot\sum_k \boldsymbol{r}_k}|\Psi_i\rangle \\ &= \sum_{\gamma,\gamma'}((C_i^{\gamma'})^* C_i^\gamma \langle\Psi_i^{\gamma'}|e^{-im_e \boldsymbol{v}\cdot\boldsymbol{r}_1}|\chi_{b_1}\rangle \mathbb{1}_{(N-1)}\langle\chi_{b_1}|e^{im_e \boldsymbol{v}\cdot\boldsymbol{a}_1}|\Psi_i^\gamma\rangle). \end{aligned} \tag{A11}$$

In the second line we have approximated $\sum_{b_2,\ldots,b_N}^{(E<E_{\rm th})} \to \sum_{b_2,\ldots,b_N}^{\text{all states}}$, as discussed in Sec. II. In going from the second to the third line we have substituted Eq. (A8) for the initial-state wave function and used the completeness of the $\{|\chi_b\rangle\}$. The identity operator that acts on the subspace of the remaining $N-1$ electrons is denoted by $\mathbb{1}_{(N-1)}$. The above expression for the semi-inclusive probability can be further simplified in specific instances. One such case is when each of the determinants that make up the initial-state wave function differ by two or more orbitals. This occurs for the group 14 (group IV) elements we consider (C, Si, Ge), where the atomic ground state has $J=0$ and in relativistic jj-coupling is a linear combination of valence configurations $(np_{1/2})^2$ and $(np_{3/2})^2$. In this case, the cross-terms in Eq. (A11) vanish and the semi-inclusive probability is

$$\begin{aligned} &p_v(|\Psi_i\rangle \to |\chi_{b_1} X_{\rm soft}\rangle) \\ &\quad\approx \sum_\gamma |C_i^\gamma|^2 \sum_{\alpha=1}^{N} |\langle\chi_{b_1}|e^{im_e \boldsymbol{v}\cdot\boldsymbol{r}}|\psi_{a_\alpha}\rangle|^2. \end{aligned} \tag{A12}$$

Finally, for the group 17 and 18 (group VII and VIII) elements the ground state wave function is described by a single Slater determinant and the semi-inclusive probability is simply given by Eq. (7).

3. Implementation in GRASP and RATIP

This appendix briefly describes our computation of the atomic wave functions using the GRASP [53–55] and RATIP [56] packages.

GRASP is an implementation of the multiconfiguration Dirac-Hartree-Fock method in which wave functions are expressed as a weighted sum of CSFs. The integrodifferential DHF equations for the radial functions are solved using finite-difference methods as part of an iterative, self-consistent field procedure. GRASP employs an exponential radial grid; we use the default value for the first grid point, $r_0 = 2.0\times10^{-6}/Z$ with Z the atomic number, and a step size in the range $h = 0.006$–0.008 depending on the element. The nuclear charge distribution is modeled by the default Fermi distribution. The Breit interaction and vacuum polarization and self-energy corrections are included in the configuration interaction.

We initially solve for the atomic ground state wave function in an optimal level calculation. The radial functions for the excited orbitals are then obtained via an extended optimal level calculation that includes configurations with a single excitation from the valence subshell. This is repeated several times, successively increasing the maximum principal quantum number, n, with all radial functions with lower n held fixed. The resulting set of radial functions is then used to construct all excited and ionized states. We therefore do not allow for relaxation of the orbitals; this is consistent with the sudden approximation employed in the derivation of the Migdal matrix element.

For ionized states, the radial functions for the continuum spinors are calculated using RATIP, which is also based on the GRASP implementation of the multiconfiguration DHF method. RATIP employs a radial grid that is exponential at small r and transitions to linear at large r. We fix the grid parameters to be $r_0 = 2.0\times10^{-6}/Z$, $h = 0.006$, and $h_p = 0.0033$. For our maximum electron energy of $E_e = 20$ keV this corresponds to 50 grid points per wavelength at large r. The continuum radial functions are each obtained in an optimal level calculation using a configuration with a single excitation from the valence subshell. This set of continuum radial functions is then used to describe all ionized states.

RATIP enforces orthogonality between the continuum wave functions and the occupied ground state orbitals.

However, the excited bound orbitals obtained using GRASP and the continuum orbitals from RATIP are not strictly orthogonal. As a result, the basis of single-electron wave functions obtained using GRASP and RATIP does not approach completeness. This does not impact the single, double, and semi-inclusive ionization probabilities we are primarily interested in, but does affect the total integrated probabilities (except for helium where the integrated probabilities can be expressed purely in terms of ground-state matrix elements). This is one of the reasons that the alternative basis-set approach of BERTHA provides a valuable cross-check of our results.

To evaluate the transition matrix elements in Sec. II and Appendix A 2, the wave functions need to be converted from the CSF basis to the determinant basis, for which we use the CESD component of RATIP. Finally, our transition probabilities include contributions up to $L = 10$ ($L = 4$ for xenon double ionization), which we find is sufficient to achieve good convergence up to the maximum recoil velocity for D-T neutrons. The one exception to this is helium, for which we include up to $L = 30$. This results in excellent convergence up to $v/\alpha \sim 6$, while from $v/\alpha = 6$ to the D-T endpoint at $v/\alpha \simeq 9.6$ conservation of probability is still maintained at the level of 4% or better.

4. Implementation in BERTHA

In this appendix we briefly describe the use of basis-set methods to compute the atomic wave functions and single-electron matrix elements, as implemented in the software package BERTHA [57].

The radial functions are expanded in a finite basis set. A conventional choice is the so-called G-spinor basis set, which takes the form

$$f^{\mathrm{L}}_{i,\kappa}(r) = N^{\mathrm{L}}_{i,\kappa} r^{\ell+1} \exp(-\lambda_{i,\kappa} r^2), \tag{A13}$$

$$\begin{aligned} f^{\mathrm{S}}_{i,\kappa}(r) &= N^{\mathrm{S}}_{i,\kappa}\left(\frac{d}{dr} + \frac{\kappa}{r}\right) f^{\mathrm{L}}_{i,\kappa}(r), \\ &= N^{\mathrm{S}'}_{i,\kappa}((\ell + \kappa + 1) - 2\lambda_{i,\kappa} r^2) r^{\ell} \exp(-\lambda_{i,\kappa} r^2), \end{aligned} \tag{A14}$$

where $N^{\mathrm{L}}_{i,\kappa}$, $N^{\mathrm{S}}_{i,\kappa}$ and $N^{\mathrm{S}'}_{i,\kappa}$ are normalization constants that prove useful in maintaining numerical accuracy in the calculation of matrix elements. The basis set parameters, $\{\lambda_{i,\kappa}\}$, are chosen following well-established practices that generate accurate bound-state energies and which approach completeness in a systematic fashion.

In this basis, the radial amplitudes are expressed in terms of the basis set by

$$P_{n,\kappa}(r) = \sum_{i=1}^{N_\kappa} c^{\mathrm{L}}_{n,\kappa,i} f^{\mathrm{L}}_{i,\kappa}(r), \tag{A15}$$

$$Q_{n,\kappa}(r) = \sum_{i=1}^{N_\kappa} c^{\mathrm{S}}_{n,\kappa,i} f^{\mathrm{S}}_{i,\kappa}(r), \tag{A16}$$

where N_κ is the rank of the expansion and $2N_\kappa$ is the dimension of the matrix representation of the Dirac operator for symmetry-type κ. The expansion coefficients are determined by the solution of a generalized matrix eigenvalue equation of the general form

$$\boldsymbol{F}_\kappa \boldsymbol{c}_{n,\kappa} = E_{n,\kappa} \boldsymbol{S}_\kappa \boldsymbol{c}_{n,\kappa}. \tag{A17}$$

The matrix $\boldsymbol{F}_\kappa$ is a matrix representation of the Dirac-Hartree-Fock operator, and includes the effects of the Coulomb interactions in the self-consistent field. The matrix $\boldsymbol{S}_\kappa$ is the block-diagonal Gram (or overlap) matrix in the given G-spinor basis set.

With this basis set, the single-electron matrix elements in Eq. (A6) can be expressed in closed form in terms of a single class of radial integral,

$$\begin{aligned} I(L, M; \zeta) &= \int_0^\infty r^M j_L(m_e v r) \exp(-\zeta r^2) dr, \\ &= \frac{(m_e v)^L}{2^{L+2}} \frac{\sqrt{\pi}}{\zeta^{(M+L+1)/2}} \frac{\Gamma(\frac{M+L+1}{2})}{\Gamma(L+\frac{3}{2})} e^{-\frac{1}{4\zeta}(m_e v)^2} \\ &\quad \times \mathcal{M}\left[\frac{L-M}{2} + 1, L + \frac{3}{2}; \frac{(m_e v)^2}{4\zeta}\right], \end{aligned} \tag{A18}$$

where $\mathcal{M}[a, b; x]$ is the confluent hypergeometric function and ζ is a real, positive parameter derived from the constituent basis set parameters λ_{ik} and $\lambda_{jk'}$. The parameters L and M are both odd or even positive integers and satisfy the subsidiary condition that $M - L$ is an even integer greater than 2, so that the confluent hypergeometric function always takes the form of a polynomial with a finite number of terms. The radial matrix elements are evaluated by taking appropriate linear combinations of the primitive integrals in Eq. (A18).

The solution of the DHF equations using G-spinors is achieved using the computer program BERTHA. For a basis set of rank N_κ, the solution of equations of the form (A17) generates a set of N_κ positive-energy states and N_κ negative-energy states for symmetry-type κ. The positive-energy states can be further categorized as being bound states if $E_{n,\kappa} < mc^2$, or virtual states if $E_{n,\kappa} > mc^2$.

APPENDIX B: COMPARISON WITH PREVIOUS CALCULATIONS

In this appendix we provide a comparison of our results for the differential single ionization probability, dp_v/dE_e, with the results from Ref. [10]. The dipole approximation is used in Ref. [10], so we make the comparison at $v = 10^{-4}$ where the dipole approximation provides accurate results.

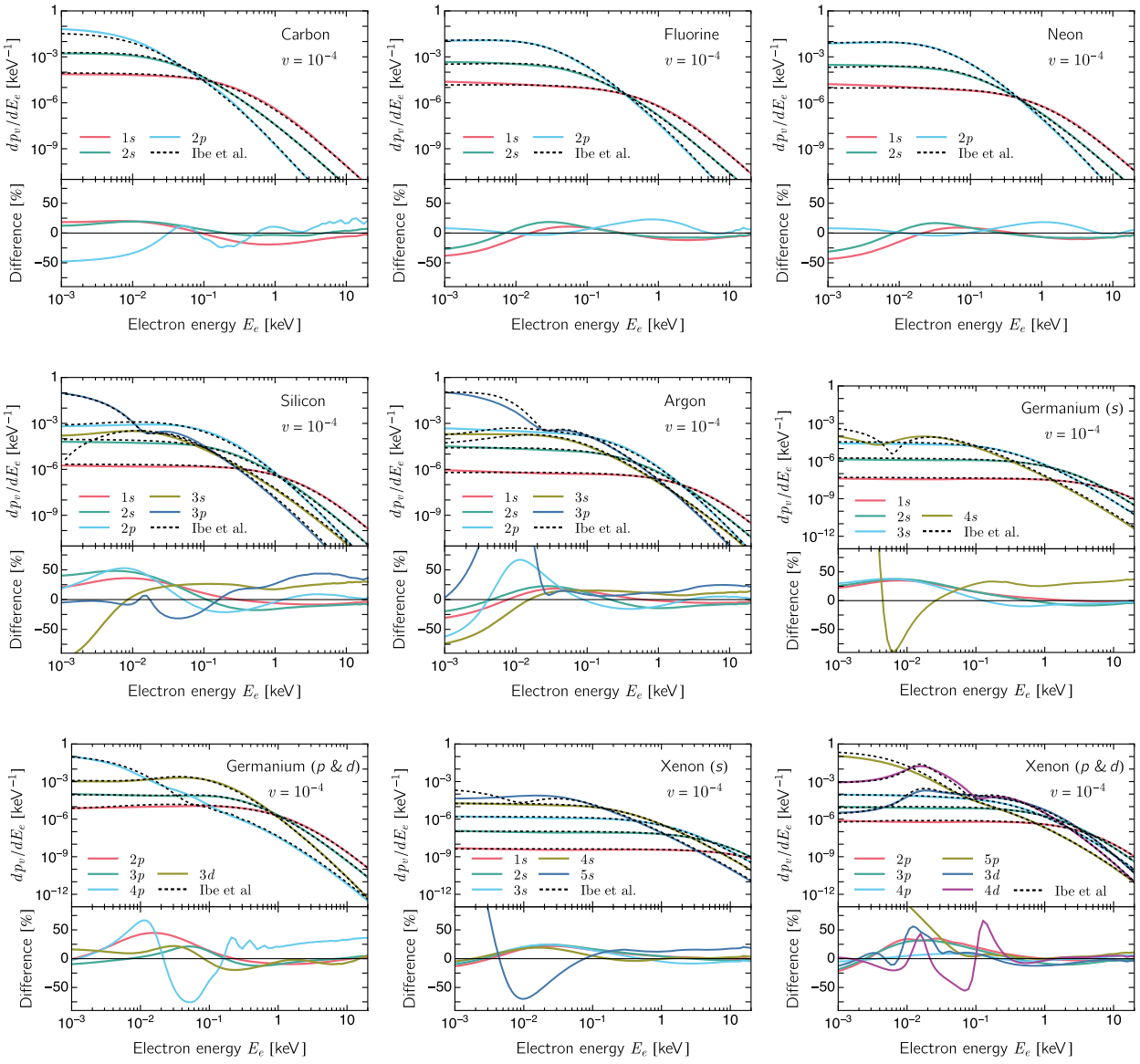

FIG. 11. The upper part of each panel compares our results (colored lines) for the differential single ionization probability, dp_v/dE_e, with the equivalent results from Ibe *et al.* [10] (dashed black lines). Following Ref. [10], we label the states with the nonrelativistic quantum numbers and, for clarity, we have separated the s and p, d states for germanium and xenon into separate panels. The lower part of each panel shows the difference, $[1/(2\pi)dp_e^c/dE_e]/[dp_v/dE_e] - 1$, expressed as a percentage.

In Fig. 11, the colored lines in the upper part of each panel show our results for ionization from each subshell in carbon, fluorine, neon, argon and xenon. The black dashed lines in each panel show the $1/(2\pi)dp^c/dE_e$ values from Ref. [10]. We use a different convention to normalize the continuum spinors, so our differential probability does not require the 2π factor. Following Ref. [10], we label the states with the nonrelativistic quantum numbers (n, ℓ). This means that the p-state probabilities are the sum of those for the $p_{1/2}$ and $p_{3/2}$ relativistic states, while the d-state probabilities are the sum of $d_{3/2}$ and $d_{5/2}$. The lower part of each panel shows $[1/(2\pi)dp_e^c/dE_e]/[dp_v/dE_e] - 1$ expressed as a percentage.

In general, we find good agreement at the level of about 30% or better across all of the atomic species. Larger departures occur but typically at very low values of the electron energy, $1\ \text{eV} \lesssim E_e \lesssim 100\ \text{eV}$, where the precise form of the potential has more of an impact. Some degree of deviation is expected since Ref. [10] employs a relativistic self-consistent mean-field approach with a local central potential, while we use the canonical Dirac-Hartree-Fock method, which includes the full nonlocal exchange potential.

APPENDIX C: NEUTRON CROSS SECTIONS

This appendix gives the neutron–nucleus cross-sections used in this work. The numerical values of the cross

TABLE I. Cross sections (in mb) for 2.47 MeV and 14.7 MeV neutrons from ENDF/B-VIII.0 [89]. The cross-sections are given for the main isotopes except for neon and xenon, where the abundance of additional isotopes is substantial ($\gtrsim$5%), so weighted averages at natural abundance are used. σ_0 denotes the total cross section, and the signal-inducing processes (σ_s) include elastic scattering (n,n), inelastic scattering (n,n'), $(n,2n)$ reactions, and radiative capture (n,γ).

	$E_n = 2.47$ MeV (D-D neutrons)						$E_n = 14.7$ MeV (D-T neutrons)					
	^{4}He	^{12}C	^{19}F	^{nat}Ne	^{40}Ar	^{nat}Xe	^{4}He	^{12}C	^{19}F	^{nat}Ne	^{40}Ar	^{nat}Xe
σ_0	3,239	1,613	3,038	2,474	5,050[a]	5,760	1,017	1,379	1,786	1,677	2,818	4,871
(n,n)	3,239	1,613	2,131	2,028	4,318[a]	3,876	1,017	895	985	771	1,556	2,933
(n,n')	...	...	907	437	731	1,869	...	426	235	240	553	464
$(n,2n)$	...	...	...	...	...	...	...	...	52	44	645	1,463
(n,γ)	...	0.05	0.09	0.10	0.32	15	...	0.15	0.03	0.02	0.08	0.72
σ_s/σ_0	100%	100%	100%	100%	100%	100%	100%	96%	71%	63%	98%	100%

[a]These cross sections are in the resonance region for ^{40}Ar(n,n) and vary rapidly with energy. The average cross sections over the range from 2.45 MeV to 2.50 MeV are $\sigma_0 = 4,327$ mb and 3,594 mb for (n,n). We use the average values in our calculations.

sections in Table I are from the ENDF/B-VIII.0 library [89]. The values on the left (right) correspond to nominal neutron energies from a D-D (D-T) neutron generator. We have listed cross sections for elastic scattering, inelastic scattering, $(n,2n)$ reactions, and radiative capture processes as all of these processes can give rise to an electron and nuclear recoil track with a common vertex: the signal for which the MIGDAL experiment is searching [48].

Figure 12 shows the combined differential cross-section for all signal-inducing processes as a function of the nuclear recoil energy. The left and right panels show the spectra expected from an incoming neutron with energy 2.47 MeV and 14.7 MeV, respectively, and the curves extend to the end-point recoil energies. The spectra were generated with GEANT4 v10.5.1 (G4NDL 4.5) [90].

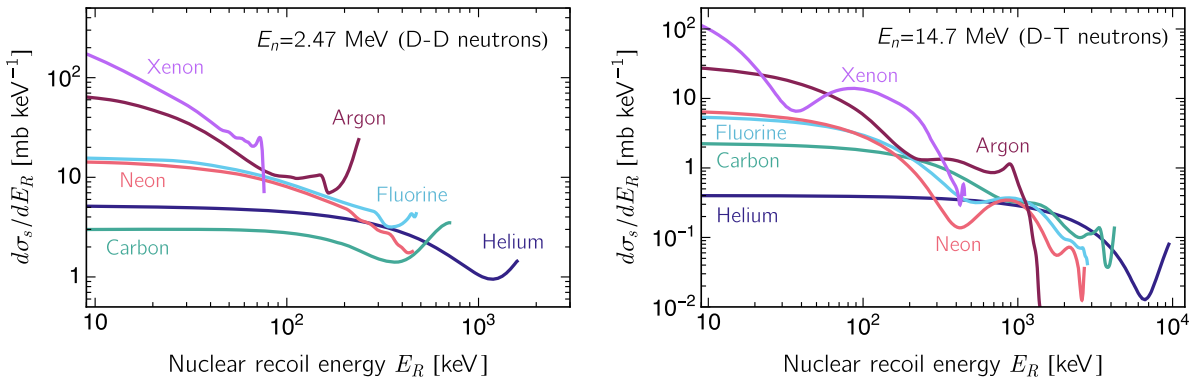

FIG. 12. Differential neutron cross sections for signal-inducing processes. The left (right) panel shows the spectra generated by a D-D (D-T) generator with neutrons at 2.47 (14.7) MeV. Each curve is drawn to the maximum recoil energy, which decreases for heavier atoms and lower neutron energy.

[1] J. Billard *et al.*, Direct detection of dark matter—APPEC committee report, Rep. Prog. Phys. **85**, 056201 (2022).
[2] J. D. Vergados and H. Ejiri, The role of ionization electrons in direct neutralino detection, Phys. Lett. B **606**, 313 (2005).
[3] C. C. Moustakidis, J. D. Vergados, and H. Ejiri, Direct dark matter detection by observing electrons produced in neutralino-nucleus collisions, Nucl. Phys. **B727**, 406 (2005).
[4] H. Ejiri, C. C. Moustakidis, and J. D. Vergados, Dark matter search by exclusive studies of X-rays following WIMPs nuclear interactions, Phys. Lett. B **639**, 218 (2006).

[5] R. Bernabei *et al.*, On electromagnetic contributions in WIMP quests, Int. J. Mod. Phys. A **22**, 3155 (2007).
[6] A. Migdal, Ionizatsiya atomov pri yadernykh reaktsiyakh, Zh. Eksp. Teor. Fiz. **9**, 1163 (1939).
[7] A. Migdal, Ionization of atoms accompanying α and β-decay, J. Phys. Acad. Sci. USSR **4**, 449 (1941).
[8] E. L. Feinberg, Ionization of the atom due to β-decay, J. Phys. Acad. Sci. USSR **4**, 423 (1941).
[9] A. B. Migdal, *Qualitative Methods in Quantum Theory* (CRC Press, Boca Ranton, 1977), 10.1201/9780429497940.
[10] M. Ibe, W. Nakano, Y. Shoji, and K. Suzuki, Migdal effect in dark matter direct detection experiments, J. High Energy Phys. 03 (2018) 194.
[11] M. J. Dolan, F. Kahlhoefer, and C. McCabe, Directly Detecting Sub-GeV Dark Matter with Electrons from Nuclear Scattering, Phys. Rev. Lett. **121**, 101801 (2018).
[12] P. Sharma, Role of nuclear charge change and nuclear recoil on shaking processes and their possible implication on physical processes, Nucl. Phys. **A968**, 326 (2017).
[13] R. Essig, J. Pradler, M. Sholapurkar, and T.-T. Yu, Relation between the Migdal Effect and Dark Matter-Electron Scattering in Isolated Atoms and Semiconductors, Phys. Rev. Lett. **124**, 021801 (2020).
[14] N. F. Bell, J. B. Dent, J. L. Newstead, S. Sabharwal, and T. J. Weiler, Migdal effect and photon bremsstrahlung in effective field theories of dark matter direct detection and coherent elastic neutrino-nucleus scattering, Phys. Rev. D **101**, 015012 (2020).
[15] D. Baxter, Y. Kahn, and G. Krnjaic, Electron ionization via dark matter-electron scattering and the Migdal effect, Phys. Rev. D **101**, 076014 (2020).
[16] S. Knapen, J. Kozaczuk, and T. Lin, Migdal Effect in Semiconductors, Phys. Rev. Lett. **127**, 081805 (2021).
[17] G. Grilli di Cortona, A. Messina, and S. Piacentini, Migdal effect and photon Bremsstrahlung: Improving the sensitivity to light dark matter of liquid argon experiments, J. High Energy Phys. 11 (2020) 034.
[18] C. P. Liu, C.-P. Wu, H.-C. Chi, and J.-W. Chen, Model-independent determination of the Migdal effect via photoabsorption, Phys. Rev. D **102**, 121303 (2020).
[19] Z.-L. Liang, C. Mo, F. Zheng, and P. Zhang, Describing the Migdal effect with a bremsstrahlung-like process and many-body effects, Phys. Rev. D **104**, 056009 (2021).
[20] N. F. Bell, J. B. Dent, B. Dutta, S. Ghosh, J. Kumar, and J. L. Newstead, Low-mass inelastic dark matter direct detection via the Migdal effect, Phys. Rev. D **104**, 076013 (2021).
[21] S. Knapen, J. Kozaczuk, and T. Lin, PYTHON package for dark matter scattering in dielectric targets, Phys. Rev. D **105**, 015014 (2022).
[22] J. F. Acevedo, J. Bramante, and A. Goodman, Accelerating composite dark matter discovery with nuclear recoils and the Migdal effect, Phys. Rev. D **105**, 023012 (2022).
[23] C. Blanco, I. Harris, Y. Kahn, B. Lillard, and J. Pérez-Ríos, The molecular Migdal effect, Phys. Rev. D **106**, 115015 (2022).
[24] M. Y. Amusia, A. S. Baltenkov, A. V. Korol, and A. V. Solov'yov, Bremsstrahlung in collisions of atoms with slow neutrons, Sov. Phys. JETP **66**, 1537 (1987).
[25] M. Y. Amusia, Atomic bremsstrahlung, Phys. Rep. **162**, 249 (1988).
[26] A. V. Korol and A. V. Solov'yov, *Polarization Bremsstrahlung* (Springer, New York, 2014), 10.1007/978-3-642-45224-6.
[27] C. Kouvaris and J. Pradler, Probing sub-GeV Dark Matter with Conventional Detectors, Phys. Rev. Lett. **118**, 031803 (2017).
[28] C. McCabe, New constraints and discovery potential of sub-GeV dark matter with xenon detectors, Phys. Rev. D **96**, 043010 (2017).
[29] D. S. Akerib *et al.* (LUX Collaboration), Results of a Search for sub-GeV Dark Matter Using 2013 LUX Data, Phys. Rev. Lett. **122**, 131301 (2019).
[30] E. Armengaud *et al.* (EDELWEISS Collaboration), Searching for low-mass dark matter particles with a massive Ge bolometer operated above-ground, Phys. Rev. D **99**, 082003 (2019).
[31] Z. Z. Liu *et al.* (CDEX Collaboration), Constraints on Spin-Independent Nucleus Scattering with sub-GeV Weakly Interacting Massive Particle Dark Matter from the CDEX-1B Experiment at the China Jinping Underground Laboratory, Phys. Rev. Lett. **123**, 161301 (2019).
[32] E. Aprile *et al.* (XENON Collaboration), Search for Light Dark Matter Interactions Enhanced by the Migdal Effect or Bremsstrahlung in XENON1T, Phys. Rev. Lett. **123**, 241803 (2019).
[33] L. Barak *et al.* (SENSEI Collaboration), SENSEI: Direct-Detection Results on sub-GeV Dark Matter from a New Skipper-CCD, Phys. Rev. Lett. **125**, 171802 (2020).
[34] G. Adhikari *et al.* (COSINE-100 Collaboration), Searching for low-mass dark matter via the Migdal effect in COSINE-100, Phys. Rev. D **105**, 042006 (2022).
[35] E. Armengaud *et al.* (EDELWEISS Collaboration), Search for sub-GeV Dark Matter via Migdal effect with an EDELWEISS germanium detector with NbSi TES sensors, Phys. Rev. D **106**, 062004 (2022).
[36] P. Agnes *et al.* (DarkSide-50 Collaboration), Search for dark matter-nucleon interactions via Migdal effect with DarkSide-50, arXiv:2207.11967.
[37] M. S. Rapaport, F. Asaro, and I. Perlman, K-shell electron shake-off accompanying alpha decay, Phys. Rev. C **11**, 1740 (1975).
[38] M. S. Rapaport, F. Asaro, and I. Perlman, L- and M-shell electron shake-off accompanying alpha decay, Phys. Rev. C **11**, 1746 (1975).
[39] H. J. Fischbeck and M. S. Freedman, Spectroscopy of α and K- and L-Electron Continua and L-Electron Pickup in ^{210}Po α Decay, Phys. Rev. Lett. **34**, 173 (1975).
[40] H. J. Fischbeck and M. S. Freedman, Angular correlation between ejected L electrons and α particles in ^{210}Po decay, Phys. Rev. A **15**, 162 (1977).
[41] F. Boehm and C. S. Wu, Internal bremsstrahlung and ionization accompanying beta decay, Phys. Rev. **93**, 518 (1954).
[42] E. Berlovich, L. Kutsentov, and V. Fleisher, Investigation of the "Jolting" of electron shells of oriented molecules containing P^{32}, J. Exp. Theor. Phys. **21**, 675 (1965).
[43] C. Couratin *et al.*, First Measurement of Pure Electron Shakeoff in the β Decay of Trapped $^6He^+$ Ions, Phys. Rev. Lett. **108**, 243201 (2012).

[44] E. Liénard *et al.*, Precision measurements with LPCTrap at GANIL, Hyperfine Interact. **236**, 1 (2015).

[45] X. Fabian *et al.*, Electron shakeoff following the β^+ decay of $^{19}Ne^+$ and $^{35}Ar^+$ trapped ions, Phys. Rev. A **97**, 023402 (2018).

[46] K. D. Nakamura, K. Miuchi, S. Kazama, Y. Shoji, M. Ibe, and W. Nakano, Detection capability of the Migdal effect for argon and xenon nuclei with position-sensitive gaseous detectors, Prog. Theor. Exp. Phys. **2021**, 013C01 (2021).

[47] N. F. Bell, J. B. Dent, R. F. Lang, J. L. Newstead, and A. C. Ritter, Observing the Migdal effect from nuclear recoils of neutral particles with liquid xenon and argon detectors, Phys. Rev. D **105**, 096015 (2022).

[48] H. M. Araújo *et al.* (MIGDAL Collaboration), The MIGDAL experiment: Measuring a rare atomic process to aid the search for dark matter, arXiv:2207.08284.

[49] J. I. Collar, A. R. L. Kavner, and C. M. Lewis, Germanium response to sub-keV nuclear recoils: A multipronged experimental characterization, Phys. Rev. D **103**, 122003 (2021).

[50] J. Liao, H. Liu, and D. Marfatia, Coherent neutrino scattering and the Migdal effect on the quenching factor, Phys. Rev. D **104**, 015005 (2021).

[51] J. Aalbers *et al.*, A next-generation liquid xenon observatory for dark matter and neutrino physics, J. Phys. G **50**, 013001 (2023).

[52] M. F. Gu, The flexible atomic code, Can. J. Phys. **86**, 675 (2008).

[53] P. Jönsson, X. He, C. Froese Fischer, and I. P. Grant, The grasp2K relativistic atomic structure package, Comput. Phys. Commun. **177**, 597 (2007).

[54] P. Jönsson, G. Gaigalas, J. Bieroń, C. Froese Fischer, and I. P. Grant, New version: Grasp2K relativistic atomic structure package, Comput. Phys. Commun. **184**, 2197 (2013).

[55] C. Froese Fischer, G. Gaigalas, P. Jönsson, and J. Bieroń, GRASP2018–A Fortran 95 version of the general relativistic atomic structure package, Comput. Phys. Commun. **237**, 184 (2019).

[56] S. Fritzsche, The RATIP program for relativistic calculations of atomic transition, ionization and recombination properties, Comput. Phys. Commun. **183**, 1525 (2012).

[57] H. M. Quiney, H. Skaane, and I. P. Grant, *Ab initio* relativistic quantum chemistry: Four-components good, two-components bad!, Adv. Quantum Chem. **32**, 1 (1998).

[58] L. Vegh, Multiple ionisation effects due to recoil in atomic collisions, J. Phys. B **16**, 4175 (1983).

[59] L. Wauters, N. Vaeck, M. Godefroid, H. W. Van Der Hart, and M. Demeur, Recoil-induced electronic excitation and ionization in one-and two-electron ions, J. Phys. B **30**, 4569 (1997).

[60] J. Berakdar, Electronic correlation studied by neutron scattering, J. Phys. B **35**, L31 (2001).

[61] J. D. Talman and A. M. Frolov, Excitations of light atoms during nuclear reactions with fast neutrons, Phys. Rev. A **73**, 032722 (2006).

[62] M. Liertzer, J. Feist, S. Nagele, and J. Burgdörfer, Multielectron Transitions Induced by Neutron Impact on Helium, Phys. Rev. Lett. **109**, 013201 (2012).

[63] M. Pindzola, T. Lee, S. A. Abdel-Naby, F. Robicheaux, J. Colgan, and M. F. Ciappina, Neutron-impact ionization of He, J. Phys. B **47**, 195202 (2014).

[64] M. Pindzola, J. Colgan, and M. Ciappina, Neutron ionization of helium near the neutron-alpha particle collision resonance, J. Phys. B **53**, 205201 (2020).

[65] S. E. Vahsen *et al.*, CYGNUS: Feasibility of a nuclear recoil observatory with directional sensitivity to dark matter and neutrinos, arXiv:2008.12587.

[66] S. E. Vahsen, C. A. J. O'Hare, and D. Loomba, Directional recoil detection, Annu. Rev. Nucl. Part. Sci. **71**, 189 (2021).

[67] L. Balogh *et al.* (NEWS-G Collaboration), The NEWS-G detector at SNOLAB, arXiv:2205.15433.

[68] L. Hamaide and C. McCabe, Fuelling the search for light dark matter-electron scattering, arXiv:2110.02985.

[69] K. Nikolopoulos *et al.* (DarkSPHERE Collaboration), DarkSPHERE: Exploring light dark matter with a spherical proportional counter electroformed underground at the Boulby underground laboratory, arXiv:2301.05183.

[70] C. E. Aalseth *et al.* (DarkSide-20k Collaboration), DarkSide-20k: A 20 tonne two-phase LAr TPC for direct dark matter detection at LNGS, Eur. Phys. J. Plus **133**, 131 (2018).

[71] P. A. Amaudruz *et al.* (DEAP-3600 Collaboration), Design and construction of the DEAP-3600 dark matter detector, Astropart. Phys. **108**, 1 (2019).

[72] D. S. Akerib *et al.* (LZ Collaboration), The LUX-ZEPLIN (LZ) experiment, Nucl. Instrum. Methods Phys. Res., Sect. A **953**, 163047 (2020).

[73] X. Cao *et al.* (PandaX Collaboration), PandaX: A liquid xenon dark matter experiment at CJPL, Sci. China Phys. Mech. Astron. **57**, 1476 (2014).

[74] E. Aprile *et al.* (XENON Collaboration), Projected WIMP sensitivity of the XENONnT dark matter experiment, J. Cosmol. Astropart. Phys. 11 (2020) 031.

[75] J. Aalbers *et al.* (DARWIN Collaboration), DARWIN: Towards the ultimate dark matter detector, J. Cosmol. Astropart. Phys. 11 (2016) 017.

[76] Z.-L. Liang, C. Mo, F. Zheng, and P. Zhang, Phonon-mediated Migdal effect in semiconductor detectors, Phys. Rev. D **106**, 043004 (2022).

[77] Migdal probabilities on GitHub, https://petercox.github.io/Migdal, Zenodo, 10.5281/zenodo.7659176.

[78] S. W. Lovesey, C. D. Bowman, and R. G. Johnson, Electron excitation in atoms and molecules by neutron-nucleus scattering, Z. Phys. B **47**, 137 (1982).

[79] Y. Kahn and T. Lin, Searches for light dark matter using condensed matter systems, Rep. Prog. Phys. **85**, 066901 (2022).

[80] H. A. Bethe and E. E. Salpeter, *Quantum Mechanics of One- and Two-Electron Atoms* (Springer, New York, 1957), 10.1007/978-3-662-12869-5.

[81] C. Froese Fischer, M. Godefroid, T. Brage, P. Jönsson, and G. Gediminas, Advanced multiconfiguration methods for complex atoms: I. Energies and wave functions, J. Phys. B **49**, 182004 (2016).

[82] J. D. Lewin and P. F. Smith, Review of mathematics, numerical factors, and corrections for dark matter experiments based on elastic nuclear recoil, Astropart. Phys. **6**, 87 (1996).

[83] D. Baxter *et al.*, Recommended conventions for reporting results from direct dark matter searches, Eur. Phys. J. C **81**, 907 (2021).

[84] C. McCabe, The Earth's velocity for direct detection experiments, J. Cosmol. Astropart. Phys. 02 (2014) 027.

[85] G. Williams, *X-Ray Data Booklet, Sec.(1.1)* (Lawrence Berkeley National Laboratory, Berkeley CA, 2009).

[86] W. Jolly, K. Bomben, and C. Eyermann, Core-electron binding energies for gaseous atoms and molecules, At. Data Nucl. Data Tables **31**, 433 (1984).

[87] P. A. M. Dirac, The quantum theory of the electron, Proc. R. Soc. A **117**, 610 (1928).

[88] *Relativistic Quantum Theory of Atoms and Molecules*, edited by I. P. Grant (Springer, New York, 2007), 10.1007/978-0-387-35069-1.

[89] D. A. Brown *et al.*, ENDF/B-VIII.0: The 8th major release of the nuclear reaction data library with CIELO-project cross sections, new standards and thermal scattering data, Nucl. Data Sheets **148**, 1 (2018).

[90] S. Agostinelli *et al.* (GEANT4 Collaboration), GEANT4-A simulation toolkit, Nucl. Instrum. Methods Phys. Res., Sect. A **506**, 250 (2003).